

# Testing independence between two random sets for the analysis of colocalization in bio-imaging

Frédéric Lavancier<sup>1,2</sup>, Thierry Pécot<sup>1</sup>, Liu Zengzhen<sup>3</sup>, and Charles Kervrann<sup>1</sup>

<sup>1</sup>Inria, Centre Rennes-Bretagne Atlantique, SERPICO Project Team, 35042 Rennes, France

<sup>2</sup>University of Nantes, Laboratoire de Mathématiques Jean Leray, 44322 Nantes, France

<sup>3</sup>Institut Curie, PSL Research University, CNRS UMR 144, Space Time Imaging of Endomembranes Dynamics Team, 75005 Paris, France

## Abstract

Colocalization aims at characterizing spatial associations between two fluorescently-tagged biomolecules by quantifying the co-occurrence and correlation between the two channels acquired in fluorescence microscopy. Colocalization is presented either as the degree of overlap between the two channels or the overlays of the red and green images, with areas of yellow indicating colocalization of the molecules. This problem remains an open issue in diffraction-limited microscopy and raises new challenges with the emergence of super-resolution imaging, a microscopic technique awarded by the 2014 Nobel prize in chemistry. We propose GcoPS, for Geo-coPositioning System, an original method that exploits the random sets structure of the tagged molecules to provide an explicit testing procedure. Our simulation study shows that GcoPS unequivocally outperforms the best competitive methods in adverse situations (noise, irregularly shaped fluorescent patterns, different optical resolutions). GcoPS is also much faster, a decisive advantage to face the huge amount of data in super-resolution imaging. We demonstrate the performances of GcoPS on two biological real datasets, obtained by conventional diffraction-limited microscopy technique and by super-resolution technique, respectively.

*Keywords:* Quantitative Fluorescence Microscopy; Spatial Statistics; Stochastic Geometry; Super-Resolution Microscopy.

# 1 Introduction

## 1.1 Biological challenge

The characterization of molecular interactions is a major challenge in quantitative microscopy. This problem is usually addressed in living cells by fluorescently labeling two types of molecules of interest with spectrally distinct fluorophores, and simultaneously imaging them. This process provides two images of the same cell, each depicting one different fluorescently tagged molecule, both corrupted with diffraction, noise and nuisance background. As an illustration, Figure 1 depicts a cell containing Langerin proteins in the red channel, along with Rab11 proteins in the green channel (Boulanger et al., 2014). Note that the figures appear in color in the electronic version of this article, and any mention of color refers to that version. In the other example of Figure 2, BDNF (brain-derived neurotrophic factor) proteins are visible in green along with vesicle markers for presynapses (vGlut) in purple (Andreska et al., 2014). These two datasets have been acquired with different microscopy techniques: 3D multi-angle TIRFM (total internal reflection fluorescence microscopy) for the image in Figure 1, and dSTORM (direct stochastic optical reconstruction microscopy) for the image in Figure 2. These data are analyzed further in Section 4 and the details of experiments are provided in the appendix.

Potential protein-protein interactions inside the cell are determined by the degree of colocalization at the resolution limit of the microscope or, in other words, by the proportion of interacting proteins co-detected at the same location or in very close proximity (Manders et al., 1993; Bolte and Cordelieres, 2006). Colocalization often corresponds to co-compartmentalization, implying that two or more molecules bind to the same structure or domain in the cell. For this reason, the analysis of colocalization is known to be a critical step in the analysis of molecular interactions. Given the observation of two types of proteins in a cell acquired by fluorescence microscopy, the main questions are whether colocalization occurs, whether it occurs globally in the whole cell or only in certain subregions of the cell, and to spatially quantify colocalization within the cell. These problems need to be correctly addressed in presence of the increasing amount of 2D, 3D, and 3D+time data available in bio-imaging. However, for the time being, there is no definitive solution to colocalization analysis, even for 2D images acquired by conventional diffraction-limited microscopy techniques.

Moreover, the emergence of super-resolution microscopy techniques such as SIM (structured illumination microscopy), dSTORM (direct stochastic optical reconstruction microscopy), PALM (photoactivated localization microscopy) and STED (stimulated emis-

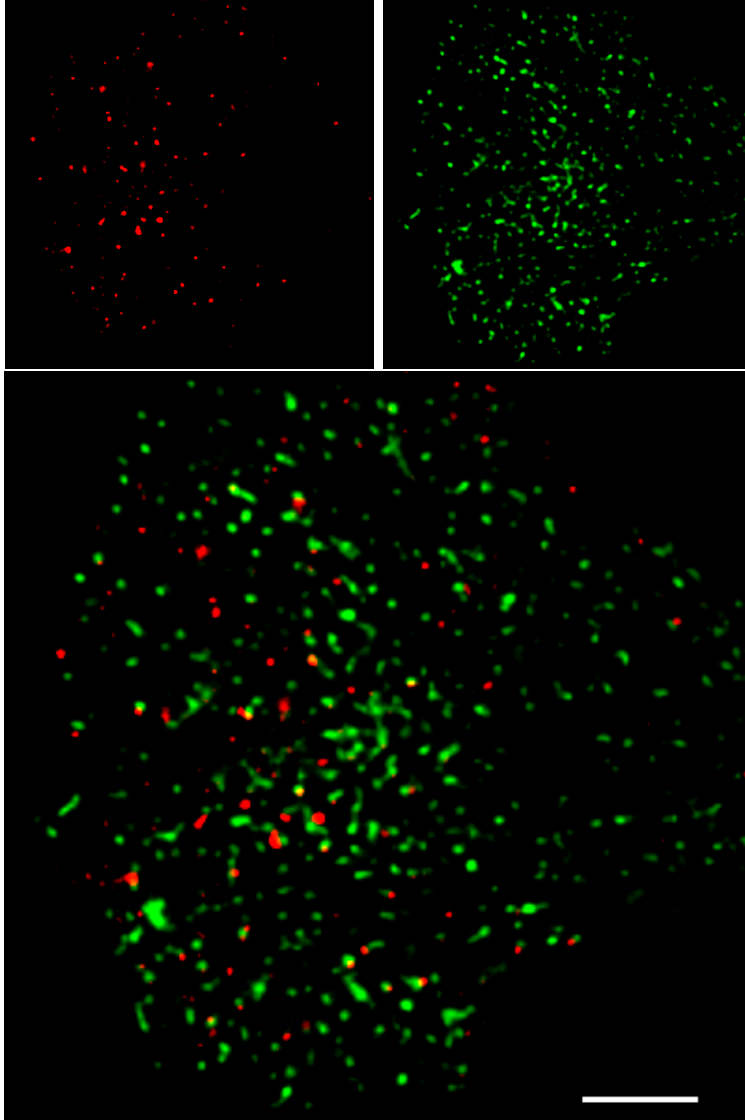


Figure 1: 3D multi-angles TIRFM acquisition of a RPE1 cell ([Boulanger et al., 2014](#)) expressing m-Cherry Langerin (red tagged molecules) and GFP Rab11 (green tagged molecules). These images are the projection (along the  $z$  axis) of the initial 3D  $400 \times 400 \times 20$  pixels images. The image at the bottom is the superposition of the two acquired images displayed at the top. The scale bar corresponds to  $10\mu\text{m}$ . This figure appears in color in the electronic version of this article, and any mention of color refers to that version.

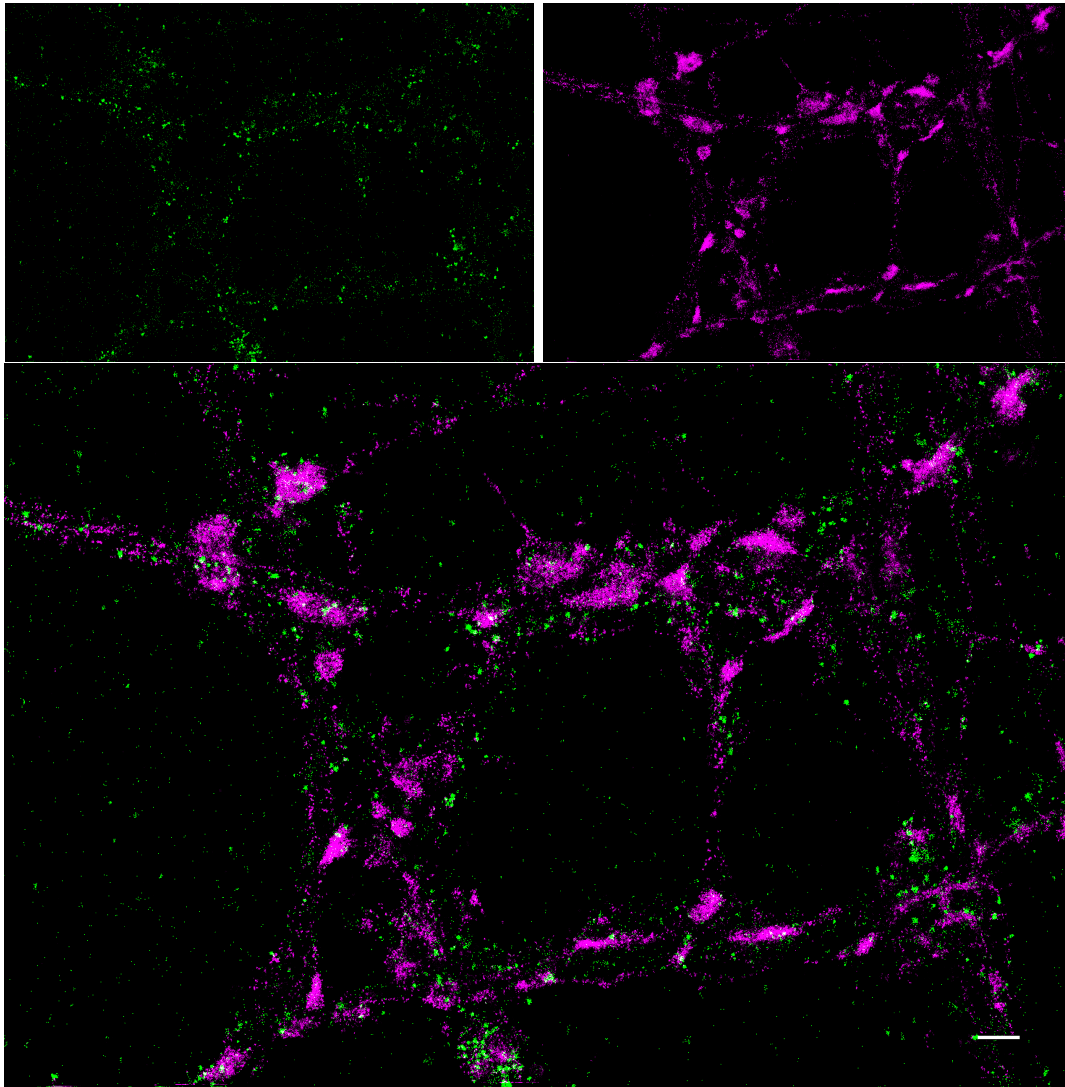


Figure 2: DSTORM acquisition of a cell from hippocampi of mice ([Andreska et al., 2014](#)) expressing BDNF proteins (green tagged molecules) and vGlut (purple tagged molecules). The image at the bottom is the superposition of the two acquired images displayed at the top. The scale bar corresponds to  $1\mu\text{m}$  and the image size is  $2547 \times 1724$  pixels. This figure appears in color in the electronic version of this article, and any mention of color refers to that version.

sion depletion) have raised supplementary challenges for the colocalization study. These techniques, whose developers Eric Betzig, William Moerner and Stefan Hell were awarded by the 2014 Nobel prize in chemistry for “the development of super-resolved fluorescence microscopy”, allow to acquire highly resolved images. This is illustrated by the data in Figure 2 obtained by dSTORM, in comparison with Figure 1 where a more conventional TIRFM was used. But the size of these highly resolved images becomes extremely large. Colocalization methods must handle these very large volumes of data efficiently. A more frequently approach is now to analyze two channels acquired by two different microscopy technologies: a conventional diffraction-limited technique (confocal, TIRFM,...) and a super-resolution technique (e.g. SIM, dSTORM, ...). This leads to situations where colocalization must be analyzed between two channels with very different resolutions (of factor 2 to 5 in practice).

## 1.2 Statistical formulation and existing methods

From a statistical perspective, detecting colocalization between two types of proteins in a cell amounts to test whether the two images acquired with fluorescence microscopy are correlated. This might appear at first sight as a basic simple statistical question. However the objects of interest, the proteins in each image, are not clearly identified. The data are two images of the same cell, corrupted by noise, nuisance background and diffraction. In the review written by [Dunn et al. \(2011\)](#), the authors conclude that “the problem of significance testing of colocalization data is one with no simple answer at this point”.

In the literature, two distinct categories of colocalization approaches are generally considered (see [Bolte and Cordelieres \(2006\)](#); [Dunn et al. \(2011\)](#) for a review): intensity-based methods and object-based methods. The former analyzes the image contents and focus on the fluorescence signals, while the latter first detect the objects of interest before analyzing their joint repartition by spatial point process statistics.

The commonly-used intensity-based technique is to simply compute the Pearson’s correlation coefficient between the two images. Nevertheless, this coefficient is sensitive to high intensity backgrounds and provides misinterpretations if the signal-to-noise ratios or the scales of the images are not similar. For these reasons and because each image is spatially autocorrelated, testing the significance of the Pearson correlation is not straightforward. A widely used solution ([Costes et al., 2004](#)) consists in block-resampling one channel, many times, in order to simulate by Monte Carlo the distribution of the Pearson’s coefficient under the null hypothesis of no-correlation. This technique is limited by the choice of the size of the blocks of pixels used for resampling, which strongly influences its result. As a

conclusion of previous works (Ramirez et al., 2010; Dunn et al., 2011), confirmed by our simulation study, this testing procedure, for the choice of blocks advised in Costes et al. (2004), leads to too many false positive colocalized situations. It also suffers from a high computational cost due to the Monte Carlo step, making this method inappropriate for modern big data. Alternative intensity-based coefficients have been proposed in the bio-imaging community, from the popular Mander’s coefficient (Manders et al., 1993) to more sophisticated ones (Comeau et al., 2008; Ramirez et al., 2010; Wu et al., 2010). These coefficients suffer from the same basic limitations as the Pearson’s coefficient, namely sensitivity to noise and to nuisance background, and heavy simulations are required to test their significance.

In the object-based methods, a segmentation procedure is applied in each image to detect the spots (or regions) in cells corresponding to the presence of proteins of interest. The detected spots are then reduced to points (their centers), providing two point patterns, and the interaction between the two point patterns is analyzed by spatial point process statistics. For this last step, assuming stationarity of the two point patterns, the most applied strategy is to analyze  $K_{12}$ , the cross Ripley’s  $K$ -function between the two point patterns. Roughly, given a point  $x$  belonging to the point pattern 1,  $K_{12}(r)$  is the expected number of points in the point pattern 2 located in a ball centered at  $x$  with radius  $r$ . If the two point patterns are independent,  $K_{12}(r)$  is simply the volume of the ball with radius  $r$  (Møller and Waagepetersen, 2004). Under some conditions, the distribution of the estimate  $\hat{K}_{12}(r)$  can be characterized asymptotically (in the sense that the spatial domain of observation is large enough) under the null hypothesis of independence, and this is exploited to construct a testing procedure for colocalization in Lagache et al. (2015). In Sherman et al. (2011), the closely related cross pair correlation function is analyzed instead of  $K_{12}$ , but no testing procedure for significance is considered. As an alternative, a parametric Gibbs model is considered in Helmuth et al. (2010) to model the interaction between the two point patterns. The significance of the Gibbs interaction is then tested by Monte Carlo simulations.

Object-based methods are less sensitive to noise and background than intensity-based techniques, though the initial segmentation step to identify the objects can be critical. Transforming each image into a point pattern is particularly well-adapted to images where the objects of interest can be fairly assimilable to points (typically small balls). The statistical analysis then becomes rigorous thanks to the well-established spatial point process techniques. However, this transformation is not suitable in presence of large or anisotropic shaped objects, in which case the reduction of each object to a single point constitutes a dramatic loss of information. For the same reason, these methods can not be applied

in subregions of the cell containing only few objects, in which case the associated point patterns would be too sparse to be analyzed. Moreover, the computational cost increases with the number of detected points and can become prohibitive in presence of high-resolved images involving a large number of objects.

### 1.3 GcoPS

We introduce a new colocalization method, detailed in Section 2, that we name GcoPS for Geo co-Positioning System. The basic idea is to analyze the two random sets composed of the detected spots obtained after a preliminary segmentation procedure in each image. Accordingly, this first step is similar to the object-based methods described before. However we do not reduce the segmented images to point patterns but keep them as they are: two binary images, each representing a random set of spots. The analysis of these random sets can then be seen as an intensity-based method, since it basically consists in testing the significance of the Pearson correlation between two binary images, see Section 2. From this perspective, GcoPS can be viewed as a compromise between an object-based method and an intensity-based method. Moreover, unlike previous intensity-based methods, our testing procedure exploits a closed formula and no Monte Carlo simulations are needed.

GcoPS has been implemented within the Icy software (de Chaumont et al., 2012), an open platform for bioimage informatics based on Java, and is available as a free downloadable module (more details at <http://icy.bioimageanalysis.org/plugin/GcoPS>). Nonetheless the C++ code is also available in the web supplement of this paper.

The rest of the paper is organized as follows. Section 2 describes the mathematical foundations of the method and explains the practical choices made for the implementation of GcoPS. Section 3 summarizes the results of our simulation study (detailed in the appendix), which demonstrates the good performances of GcoPS in comparison to the most used intensity-based method of Costes et al. (2004) and to the object-based method of Lagache et al. (2015) that exploits the cross Ripley’s  $K$ -function. In Section 4, we apply GcoPS to the analysis of the real datasets presented in Section 1.1. A concluding discussion is made in Section 5. Finally a supporting information, available in the appendix of this paper, contains the most technical aspects of our contribution, the detailed results of the simulation study, the specificities of data preparation and supplementary figures.

## 2 The method

### 2.1 Mathematical foundations

GcoPS applies a test on a binary image pair as explained in this section. The two binary images are obtained by segmenting the input fluorescence images. This splits the set of pixels into a background set and a foreground set, both of which should be non-empty. The sensitivity to this preliminary step is analyzed in Section 3, where GcoPS is seen to be robust to the choice of the segmentation algorithm.

In what follows, we view the two foreground sets of the two binary images as realizations of two random sets observed through a pixelated image. We refer to Chiu et al. (2013) for basic notions on random sets. Formally, let  $\Gamma_1 \subset \mathbb{Z}^d$  and  $\Gamma_2 \subset \mathbb{Z}^d$  be two random sets in  $\mathbb{Z}^d$ , where  $d$  stands for the dimension (typically  $d = 2$  or  $d = 3$  in our examples). Intuitively,  $\Gamma_1$  would be the foreground set of the first image if this image was supported on the infinite lattice  $\mathbb{Z}^d$ , and similarly for  $\Gamma_2$ . We let  $\Omega_n \subset \mathbb{Z}^d$  be the observation region of these random sets, that is the region of interest of the observed images. The index  $n$  stands for the number of elements (pixels or voxels) in  $\Omega_n$ , or in other words its cardinality. For instance when  $d = 2$ , if the region of interest is the whole observed images of size  $n_1 \times n_2$  pixels,  $\Omega_n$  is simply the lattice  $\{1, \dots, n_1\} \times \{1, \dots, n_2\}$  with  $n = n_1 n_2$  pixels. In general yet, the region of interest  $\Omega_n$  is a subregion of the observed images, see for instance Figure 1. The two observed foreground sets are therefore  $\Gamma_1 \cap \Omega_n$  and  $\Gamma_2 \cap \Omega_n$ . In the following we develop a procedure to test whether  $\Gamma_1$  and  $\Gamma_2$  are independent or not (the case of colocalization), based on the observation of  $\Gamma_1 \cap \Omega_n$  and  $\Gamma_2 \cap \Omega_n$  and when  $n \rightarrow \infty$ .

Let us consider, for a generic given point  $o \in \mathbb{Z}^d$ , the probabilities

$$p_1 = \mathbb{P}(o \in \Gamma_1), \quad p_2 = \mathbb{P}(o \in \Gamma_2), \quad p_{12} = \mathbb{P}(o \in \Gamma_1 \cap \Gamma_2). \quad (2.1)$$

If  $\Gamma_1$  and  $\Gamma_2$  are two independent random sets, we have  $p_{12} = p_1 p_2$ . A natural empirical measure of the departure from independence between  $\Gamma_1$  and  $\Gamma_2$  is therefore

$$\hat{D}_n = \hat{p}_{12} - \hat{p}_1 \hat{p}_2, \quad (2.2)$$

where

$$\hat{p}_1 = \frac{1}{n} |\Gamma_1 \cap \Omega_n|, \quad \hat{p}_2 = \frac{1}{n} |\Gamma_2 \cap \Omega_n|, \quad \hat{p}_{12} = \frac{1}{n} |\Gamma_1 \cap \Gamma_2 \cap \Omega_n|,$$

where  $|A|$  denotes the number of elements in a finite subset  $A$  of  $\mathbb{Z}^d$ . Note that  $\hat{p}_1$  is simply the mean number of “red” pixels in the region of interest, while  $\hat{p}_2$  is the mean number of “green” pixels and  $\hat{p}_{12}$  is the mean number of “yellow” pixels (that are both “green” and

“red”). The following proposition is the basic result for our testing procedure. It provides a central limit theorem for  $\hat{D}_n$  when  $\Gamma_1$  and  $\Gamma_2$  are independent.

To this end, we assume that  $\Gamma_1$  and  $\Gamma_2$  are stationary sets. Denoting by  $\Gamma_1 - h$  the translation of  $\Gamma_1$  by the vector  $h \in \mathbb{Z}^d$ , this means that the distribution of  $\Gamma_1$  is the same as the distribution of  $\Gamma_1 - h$  for any  $h \in \mathbb{Z}^d$ , and similarly for  $\Gamma_2$ . We denote by  $C_1$  and  $C_2$  the auto-covariance functions of  $\Gamma_1$  and  $\Gamma_2$ , respectively. Specifically, denoting by  $\mathbf{1}_{\Gamma_1}(x)$  the indicator function equal to 1 if  $x \in \Gamma_1$  and to 0 otherwise,  $C_1(h)$  is defined for any  $h \in \mathbb{Z}^d$  and any  $x \in \mathbb{Z}^d$  by

$$\begin{aligned} C_1(h) &= \mathbb{E}\{\mathbf{1}_{\Gamma_1}(x)\mathbf{1}_{\Gamma_1}(x+h)\} - \mathbb{E}\{\mathbf{1}_{\Gamma_1}(x)\}\mathbb{E}\{\mathbf{1}_{\Gamma_1}(x+h)\} \\ &= \mathbb{P}\{o \in \Gamma_1 \cap (\Gamma_1 - h)\} - p_1^2. \end{aligned}$$

This expression does not depend on  $x$  by stationarity of  $\Gamma_1$  but involves the probability that two points separated by  $h$  belong to  $\Gamma_1$ . In particular  $C_1(0) = p_1(1 - p_1)$ . The formulas for  $C_2$  are the same where  $\Gamma_1$  is replaced by  $\Gamma_2$ , and  $p_1$  by  $p_2$ . If we assume further that the distribution of  $\Gamma_1$  and  $\Gamma_2$  are invariant by rotation, then  $C_1$  and  $C_2$  are isotropic and only depend on the norm  $\|h\|$ . Our procedure only assumes stationarity but not necessarily isotropy, which makes it adapted to situations in bio-imaging where the observed molecules do not have an isotropic shape. The covariance functions can be estimated by the empirical auto-covariance functions  $\hat{C}_1$  and  $\hat{C}_2$  based on the observation of  $\Gamma_1 \cap \Omega_n$  and  $\Gamma_2 \cap \Omega_n$ . For  $h \in \mathbb{Z}^d$ , let  $\Lambda_n(h) = \{x \in \Omega_n, y \in \Omega_n \text{ such that } y = x + h\}$ . A standard expression of  $\hat{C}_1(h)$  is given by

$$\hat{C}_1(h) = \frac{1}{|\Lambda_n(h)|} \sum_{x \in \Omega_n} \sum_{y \in \Omega_n} \{\mathbf{1}_{\Gamma_1}(x) - \hat{p}_1\} \{\mathbf{1}_{\Gamma_1}(y) - \hat{p}_1\} \mathbf{1}_{x-y=h}, \quad (2.3)$$

if  $\Lambda_n(h) \neq \emptyset$ , and  $\hat{C}_1(h) = 0$  otherwise, see for instance [Cressie \(1991\)](#). This estimator is a good approximation of  $C_1(h)$  whenever  $|\Lambda_n(h)|$  is not too small. Robust or tapered estimators of  $C_1(h)$  can also be used to reduce the bias ([Cressie, 1991](#); [Guyon, 1995](#)). From a theoretical point of view, we can use any estimator of  $C_1(h)$  (and similarly for  $C_2(h)$ ) in [Proposition 1](#), provided it is consistent for all  $h \in \mathbb{Z}^d$ , which is in particular the case of [\(2.3\)](#) under our assumptions ([Guyon, 1995](#), Theorem 4.1.1).

To state our central limit theorem, we need to assume that the observation domain  $\Omega_n$  is a *regular* finite subset of  $\mathbb{Z}^d$ , which means that  $n^{-1}|\partial\Omega_n| \rightarrow 0$  as  $n \rightarrow \infty$  where  $\partial\Omega_n$  denotes the boundary of  $\Omega_n$ . This assumption is not restrictive and holds true if, for instance,  $\Omega_n$  contains a square lattice with side-length  $n_0$  and  $n_0 \rightarrow \infty$  as  $n \rightarrow \infty$ .

Moreover, we assume that  $\Gamma_1$  and  $\Gamma_2$  are two  $R$ -dependent stationary random sets. We recall that  $\Gamma_1$  is  $R$ -dependent if the events  $\mathbf{1}_{\Gamma_1}(x)$  and  $\mathbf{1}_{\Gamma_1}(y)$  are independent whenever  $x$  and  $y$  are separated by a distance greater than  $R$ . In this case, if  $\|h\| \geq R$  then  $C_1(h) = 0$  and  $C_2(h) = 0$ . This theoretical framework guarantees the weak spatial dependence of  $\Gamma_1$  and  $\Gamma_2$ , but in practice the value of  $R$  does not need to be known, see Remark 2.2. This assumption could be weakened to strong mixing conditions as in Bolthausen (1982), but at the cost of slightly more technicalities that we prefer to omit. This would amount to control the rate of convergence to 0 of  $C_1(h)$  and  $C_2(h)$  when  $\|h\| \rightarrow \infty$ . Nonetheless,  $R$ -dependency is a reasonable assumption for applications in bio-imaging, which provides insightful results. It is for instance fulfilled if  $\Gamma_1$  and  $\Gamma_2$  are Boolean germ-grain models with bounded radii (Gotze et al., 1995).

Under these assumptions, we prove in the following proposition that the variance of  $\hat{D}_n$  is equivalent to  $n^{-1}S$  with

$$S = \sum_{h \in \mathbb{Z}^d} C_1(h)C_2(h) = \sum_{h \in \mathbb{Z}^d, \|h\| \leq R} C_1(h)C_2(h), \quad (2.4)$$

where the last simplification comes from the  $R$ -dependent assumption we made. Our test statistic is finally

$$T_n = \sqrt{n} \frac{\hat{D}_n}{\sqrt{\hat{S}_n(\delta)}}, \quad (2.5)$$

where  $\hat{S}_n(\delta)$  estimates  $S$  and is given for  $\delta > 0$  by

$$\hat{S}_n(\delta) = \sum_{h \in \mathbb{Z}^d, \|h\| \leq \delta} \hat{C}_1(h)\hat{C}_2(h).$$

Note that if  $\hat{C}_1(h)$  and  $\hat{C}_2(h)$  are consistent estimators,  $\hat{S}_n(\delta)$  is a consistent estimator of  $S$  whenever  $\delta \geq R$ . We are now in position to state our main result. Its proof is postponed to the appendix.

**Proposition 1.** *Let  $\Gamma_1$  and  $\Gamma_2$  be two  $R$ -dependent stationary random sets on  $\mathbb{Z}^d$  with autocovariance functions  $C_1$  and  $C_2$ , respectively, satisfying  $S > 0$  where  $S$  is defined in (2.4). Assume that  $\Omega_n$  is a regular finite subset of  $\mathbb{Z}^d$  with cardinality  $n$  and that  $\hat{C}_1(h)$  and  $\hat{C}_2(h)$  are consistent estimators of  $C_1(h)$  and  $C_2(h)$  for any  $h \in \mathbb{Z}^d$ . Let  $T_n$  be defined by (2.5) with  $\delta \geq R$ . If  $\Gamma_1$  and  $\Gamma_2$  are independent, then  $T_n$  tends in distribution to a standard Normal variable as  $n \rightarrow \infty$ .*

**Remark 2.1.** *The statistic  $T_n$  can be viewed as a normalized version of the empirical Pearson correlation between the two binary images  $(\mathbf{1}_{\Gamma_1}(x))_{x \in \Omega_n}$  and  $(\mathbf{1}_{\Gamma_2}(x))_{x \in \Omega_n}$ . From this point of view, our approach shares some similarities with the Costes method (Costes et al., 2004), where the correlation between the two raw images is tested by Monte Carlo simulations. The two important differences are that we consider binary images instead of the raw images, which limit the noise and background effects, and that we know the asymptotic distribution of  $T_n$ , which avoids Monte Carlo simulations.*

**Remark 2.2.** *We assume that  $\Gamma_1$  and  $\Gamma_2$  are  $R$ -dependent but  $R$  does not need to be known. This assumption is a convenient way to capture the spatial weak dependence of the random sets. Under a more general setting of weak dependence, the statement would be similar although the proof would require more technicalities. A key point is that  $\hat{S}_n(\delta)$  must be a consistent estimator of  $S$ . This is in general true for a proper choice of  $\delta = \delta_n$  depending on  $n$ . Specifically,  $\delta_n$  needs to tend to  $\infty$  but slower than  $n$ . This choice of  $\delta$  corresponds to the choice of the bandwidth (or truncation parameter) for the HAC (heteroskedasticity and autocorrelation consistent) estimator in econometry, see for instance Andrews (1991). For  $R$ -dependent random sets,  $\delta_n \geq R$  is sufficient. The practical way of choosing  $\delta$ , detailed in the next section, applies for any weak dependent random sets and does not depend on the  $R$ -dependent assumption.*

## 2.2 Implementation of GcoPS

The testing procedure for colocalization in  $\Omega_n$  boils down to a test of independence between  $\Gamma_1 \cap \Omega_n$  and  $\Gamma_2 \cap \Omega_n$ , which is straightforwardly deduced from Proposition 1: The null hypothesis of independence is rejected at the asymptotic level  $\alpha \in (0, 1)$  if  $|T_n| > q(\alpha/2)$  where  $q(\alpha/2)$  denotes the upper  $\alpha/2$ -quantile of the standard normal distribution. The corresponding  $p$ -value is

$$p\text{-value} = 2(1 - \Phi(|T_n|)), \quad (2.6)$$

where  $\Phi$  denotes the cumulative distribution function of the standard normal distribution. This bilateral test can be modified into a unilateral test if the focus for the alternative hypothesis is more specifically colocalization (*resp.* anti-colocalization), that is positive (*resp.* negative) dependence between  $\Gamma_1$  and  $\Gamma_2$ , rather than dependence in a general sense. Then a more powerful procedure at the asymptotic level  $\alpha$  consists in rejecting the null when  $T_n > q(\alpha)$  (*resp.*  $T_n < -q(\alpha)$ ), which corresponds to  $p\text{-value} = 1 - \Phi(T_n)$  (*resp.*  $p\text{-value} = \Phi(T_n)$ ).

In the module GcoPS of Icy and in the experiments of the next section, we did the following choices of implementation. The empirical covariances  $\hat{C}_1$  and  $\hat{C}_2$  are obtained

by an FFT (Fast Fourier Transform) in each image. Concerning the truncation parameter  $\delta$  in  $\hat{S}_n(\delta)$ , we choose the larger value of  $\|h\|$  such that both  $\hat{C}_1(h)/\hat{C}_1(0) > 0.1$  and  $\hat{C}_2(h)/\hat{C}_2(0) > 0.1$ . In other words,  $\delta$  is the maximal range of empirical correlation in  $\Gamma_1$  and  $\Gamma_2$  beyond which the correlation is less than 0.1. Beyond this range  $\delta$ , we view the values of  $\hat{C}_1(h)\hat{C}_2(h)$  as a nuisance noise. This choice of truncation has also the advantage to speed up the computation in comparison with a larger choice of  $\delta$ . Finally,  $\hat{p}_1$ ,  $\hat{p}_2$  and  $\hat{p}_{12}$  are immediately obtained from the mean of the binary images  $(\mathbf{1}_{\Gamma_1}(x))_{x \in \Omega_n}$  and  $(\mathbf{1}_{\Gamma_2}(x))_{x \in \Omega_n}$ , and from their product. This implementation ensures a very low computational cost, as attested by the results discussed in Section 3 and reported in the appendix.

### 3 Evaluation on synthetic data sets

We evaluate in this section the performance of GcoPS on 2D and 3D data sets in adverse and noisy situations and compare it to the competitive Costes method (Costes et al., 2004), the most used intensity-based method in bio-imaging, and to the object-based method of Lagache et al. (2015), which relies on the analysis of the cross Ripley’s  $K$ -function. The results of our simulations are detailed in the appendix. In summary we have assessed the following aspects:

1. Computation time in 2D, 2D+time and 3D data;
2. Performances on simulated 2D images, possibly corrupted with noise and a spatial shift;
3. Sensitivity to image segmentation;
4. Sensitivity to the shape and scale of objects;
5. Performances in presence of a different optical resolution in each image;
6. Performances on simulated 3D images.

Figure 3 shows examples of image pairs that we have evaluated with each method. This figure demonstrates the diversity of the considered situations. Note that the displayed images pairs come from independent channels, but we obviously also considered correlated channels in each situation. In each case, a thousand of image pairs have been simulated to evaluate the methods. We refer to the appendix for details about the image generators, more pictures and thorough comments.

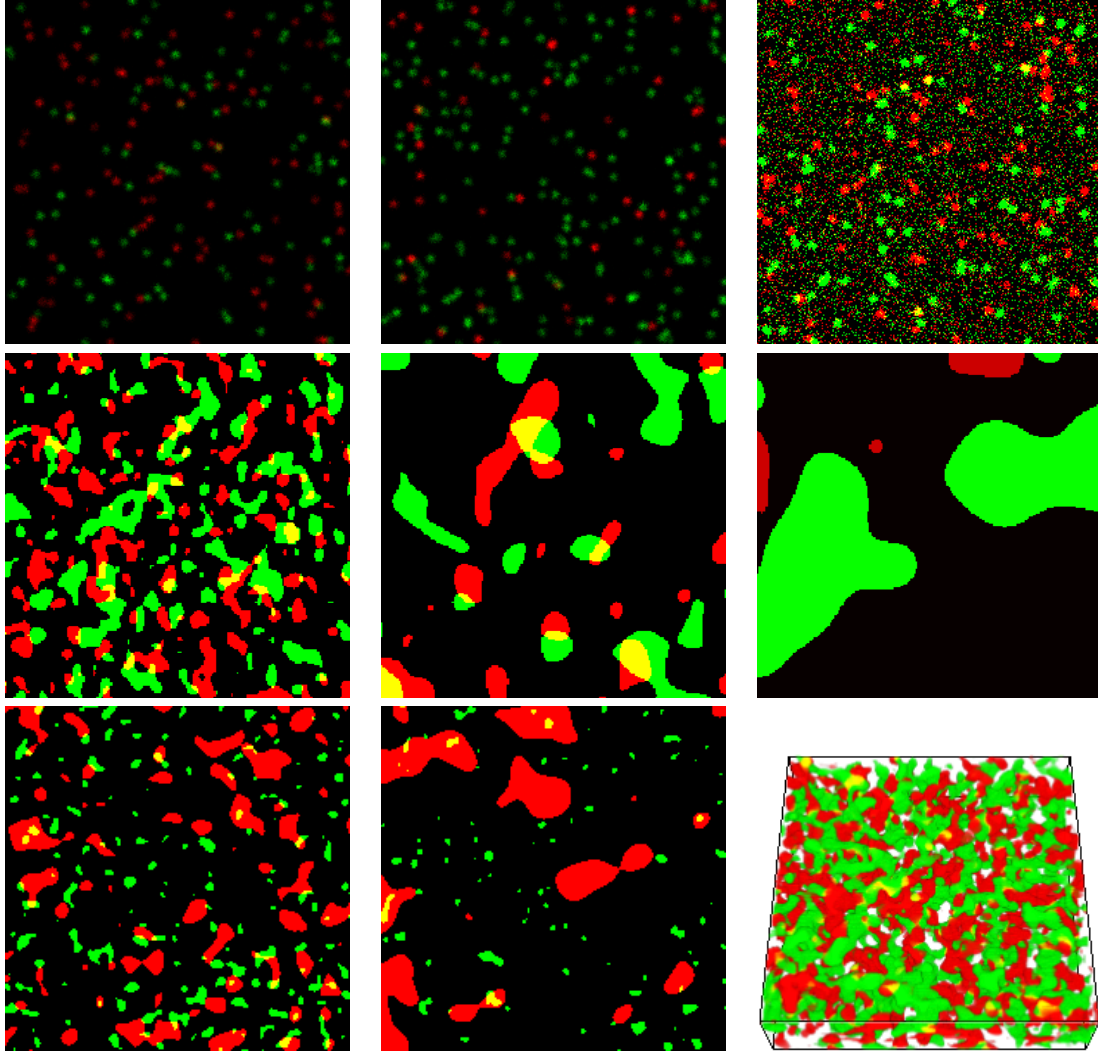


Figure 3: Examples of simulated image pairs used to evaluate the performances of GcoPS. From top left to bottom right: i) 2D image possibly corrupted with noise and a spatial shift; ii) 2D image where the green channel shows 4 times more objects than the red channel; iii) over-segmented image; iv)-vi) various shapes and scales of objects; vii)-viii) different optical resolution in each channel; ix) 3D image. This figure appears in color in the electronic version of this article, and any mention of color refers to that version.

In a nutshell, our simulation study reveals that the main drawbacks of the Costes method is the computational time due to its Monte Carlo step, that can be cumbersome for 2D+time and 3D images, along with too many false positive decisions (12% in average and up to 25%, instead of the expected 5% when the level of the test is fixed to 0.05). On the other hand, the main weakness of the object-based method of [Lagache et al. \(2015\)](#) is the lack of sensitivity to colocalization. This clearly appears in presence of large objects (as in the rightmost plot of the middle row of [Figure 3](#)), a situation where reducing each object to a point is improper. This method is also very sensitive to the preliminary segmentation step. In particular it completely fails to detect colocalization for over-segmented images (as in the top right plot of [Figure 3](#)). In turn, GcoPS does not suffer from the aforementioned drawbacks: i) it is fast; ii) it well controls the probability of false positives; iii) it is very sensitive to colocalization; and iv) it is robust to segmentation, to the shape and the size of the objects, and to a possible different optical resolution in each channel.

An important consequence of the good performance of GcoPS in presence of large objects is that this method can be applied in small windows in the image. Indeed, dividing images into sub-regions acts as enlarging objects, a situation GcoPS handles well. This opens the possibility to accurately localize colocalization. Moreover, the robustness of GcoPS in presence of a different optical resolution in each image (as in the leftmost plot of the bottom row of [Figure 3](#)) shows that GcoPS is also able to efficiently process images for which a different microscopy technique is used for detecting each type of molecules.

## 4 Application to real biological imaging

### 4.1 Spatiotemporal colocalization of Langerin and Rab11a in 3D-TIRFM

In the first experiment, a temporal acquisition with 3D-TIRFM was performed ([Boulanger et al., 2014](#)) using wild-type RPE1 cells transfected with Langerin-mCherry and Rab11a-GFP, resulting in 35 frames of image pairs with a size equal to  $400 \times 400 \times 20$  pixels. The details of data preparation are provided in the appendix. [Figure 1](#) depicts the two images obtained at time  $t = 0$  (that is the first frame) along with their superposition, once projected along the  $z$  axis. The same superposition is shown again in [Figure 4 \(a\)](#). The value of the test statistic  $T_n$  of [Proposition 1](#) (that we alternatively name colocalization score) computed on the whole cell is very large (about 28), whatever the frame considered in the sequence is, showing a clear colocalization between the two channels. We then

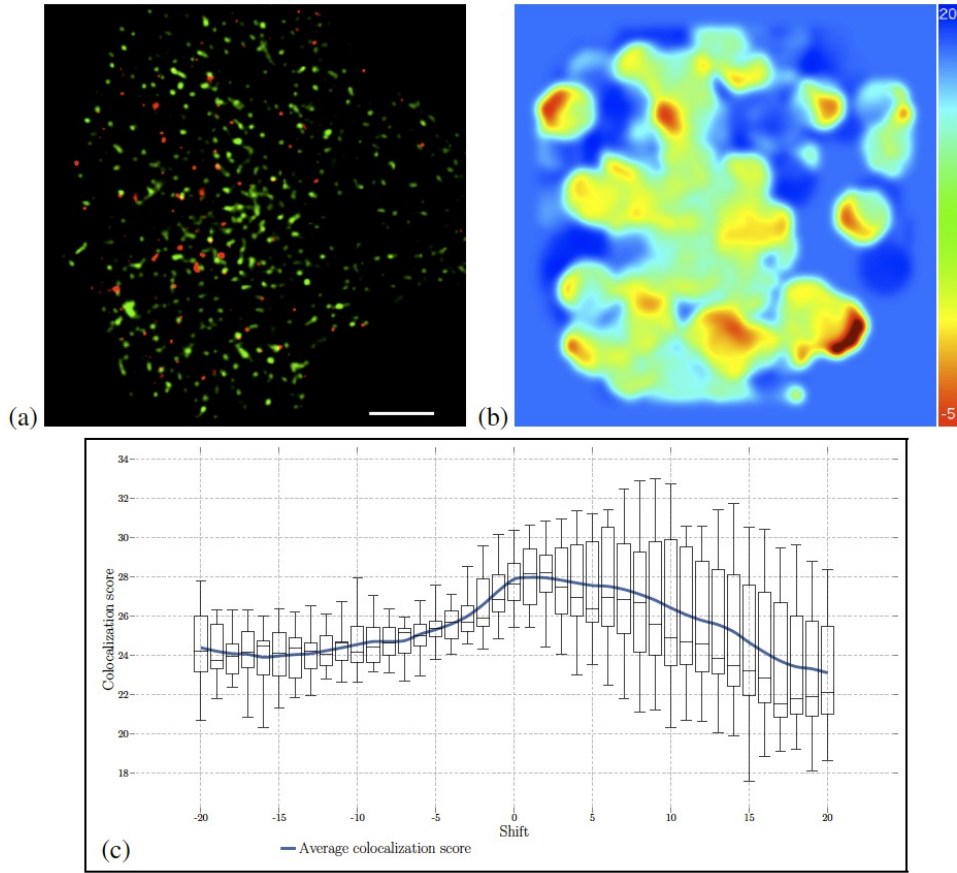


Figure 4: Spatiotemporal colocalization of Langerin and Rab11a proteins in a 3D multi-angles TIRF acquisition (Boulanger et al., 2014) providing 35 frames of image pairs with a size equal to  $400 \times 400 \times 20$  pixels. (a) Average intensity projection (along the  $z$  axis) of a 3D multi-angles TIRF acquisition (Boulanger et al., 2014) at time  $t = 0$  showing a RPE1 cell expressing m-Cherry Langerin (red channel) and GFP Rab11 (green channel) on a crossbow shaped micropattern. The scale bar corresponds to  $10 \mu\text{m}$ . (b) Heat map for continuous visualization of colocalization score associated to the left image at time  $t = 0$ . (c) Distribution of colocalization scores (box plots) and their averages (blue solid line) between pairs of images taken at time  $t$  and  $t \pm \Delta t$ , for a set of temporal shifts  $\Delta t \in \{-20, \dots, 20\}$  and computed over the 35 frames ( $t \in \{0, \dots, 34\}$ ) as displayed at the top at  $t = 0$ . This figure appears in color in the electronic version of this article, and any mention of color refers to that version.

processed a dense colocalization map at time  $t = 0$ , see Figure 4 (b), by computing the colocalization score  $T_n$  every 25 pixels at the medium plane on windows of size  $50 \times 50 \times 10$  voxels. The spatial density of colocalization scores is computed by applying a Gaussian kernel density method with a global bandwidth equal to 5. This representation has the advantage to discriminate between different levels of colocalization since a more colocalized region will have a higher colocalization score.

Finally, we applied GcoPS to the whole Langerin-mCherry/Rab11a-GFP image pair sequence, frame by frame, to get the distribution of the colocalization score  $T_n$ . Next, we shifted the frames between the two channels and applied GcoPS from -20 to +20 frames shift by considering Langerin-mCherry as the reference. The mean colocalization scores along with their distributions are reported for each temporal shift in Figure 4 (c). The slope of the colocalization scores is steeper for a positive temporal shift than for a negative temporal shift, demonstrating that globally, Rab11a is visible before Langerin, which is consistent with previous observations (Gidon et al., 2012; Boulanger et al., 2014).

## 4.2 Colocalization of BDNF proteins and vGlut in dSTORM

In the second experiment, we evaluated the colocalization between BDNF (brain-derived neurotrophic factor) proteins and vGlut, a vesicle marker for presynapses, on an image acquired with dSTORM (Andreska et al., 2014), see Figure 2. While identifying BDNF proteins is straightforward with a standard spot detector, the segmentation of vGlut is more difficult as these markers do not correspond to regular shapes. Consequently, we performed three different segmentations by thresholding the image with three different thresholds, resulting in the three binary images shown in the appendix. The  $p$ -value obtained with GcoPS is extremely low ( $p$ -value = 0) for the three segmentations of vGlut, a result consistent with previously published studies (Andreska et al., 2014) where colocalization between BDNF proteins and vGlut was unraveled. The object-based method of Lagache et al. (2015) needs a segmentation of vGlut with a high threshold to obtain a low  $p$ -value ( $p$ -value = 0.005). Segmentations with low thresholds give large objects, leading to a failure for this method ( $p$ -value = 0.532 and  $p$ -value = 0.061). The intensity-based method of Costes et al. (2004) provides  $p$ -values close to 0 whenever the size of blocks for the permutation step is fixed to  $2 \times 2$ , or  $5 \times 5$  or  $10 \times 10$  pixels<sup>2</sup> in the two channels. This result is in agreement with the conclusion of GcoPS. However the Costes method needs about 3 minutes to process this pair of images while GcoPS only takes 9 seconds. Nonetheless, it is fair to recall that all these methods assume stationarity of distributions of the proteins in the two channels. This assumption is not satisfied here and one must be

careful with the previous conclusions.

We then applied GcoPS to windows of size  $50 \times 50$  pixels randomly located in the subregion of the image containing the segmented objects to identify the regions of colocalization (see the examples at the bottom of Figure 5). The colocalization regions identified by GcoPS are represented as white circles (the centers of the tested windows) in Figure 5. The window size is here chosen sufficiently small to analyze local interactions in detail, while being sufficiently large with respect to the size of the objects to safely apply our testing procedure. Note that the distribution of proteins in these local windows can be more reasonably considered to be stationary, unlike the distribution in the whole image. This representation of colocalization hits, based on tests carried out on randomly located windows, is a fastest alternative to the dense colocalization map shown in Figure 4, that requires to process the testing procedure on all local windows. The two possibilities to analyze local interactions are included in the GcoPS module of Icy.

## 5 Discussion

We developed GcoPS, an original, fast and robust approach to test and quantify interactions between molecules. Given a pair of binary images, obtained by segmentation of the input fluorescence images, GcoPS tests if they are independent or not, at the whole image scale and in image subregions. This testing procedure exploits the fact that these binary images can be viewed as realizations of random sets.

GcoPS can be viewed as a compromise between an object-based method and an intensity-based method. As demonstrated by the simulation study summarized in Section 3 and detailed in the appendix, it benefits from the advantages of both approaches while avoiding their weaknesses. Indeed, GcoPS is robust to noise and to nuisance background, inheriting the merits of an object-based method. But since the objects are not simply reduced to points, GcoPS is adapted to any kind of object shapes and sizes. For the same reason, it is more powerful to test colocalization in small subregions of the cell than a point pattern approach, that would only be based on a few points. This property opens the possibility to efficiently localize the colocalization between markers within the cell. GcoPS is also able to evaluate the colocalization between large objects and small dots, as in a composite TIRF-PALM experiment. Finally, since the analysis of random sets boils down to the analysis of binary images, GcoPS is very fast, with no dependence on the number of objects per image, unlike spatial point process statistics.

A natural concern may be the sensitivity of the method to the preliminary segmentation

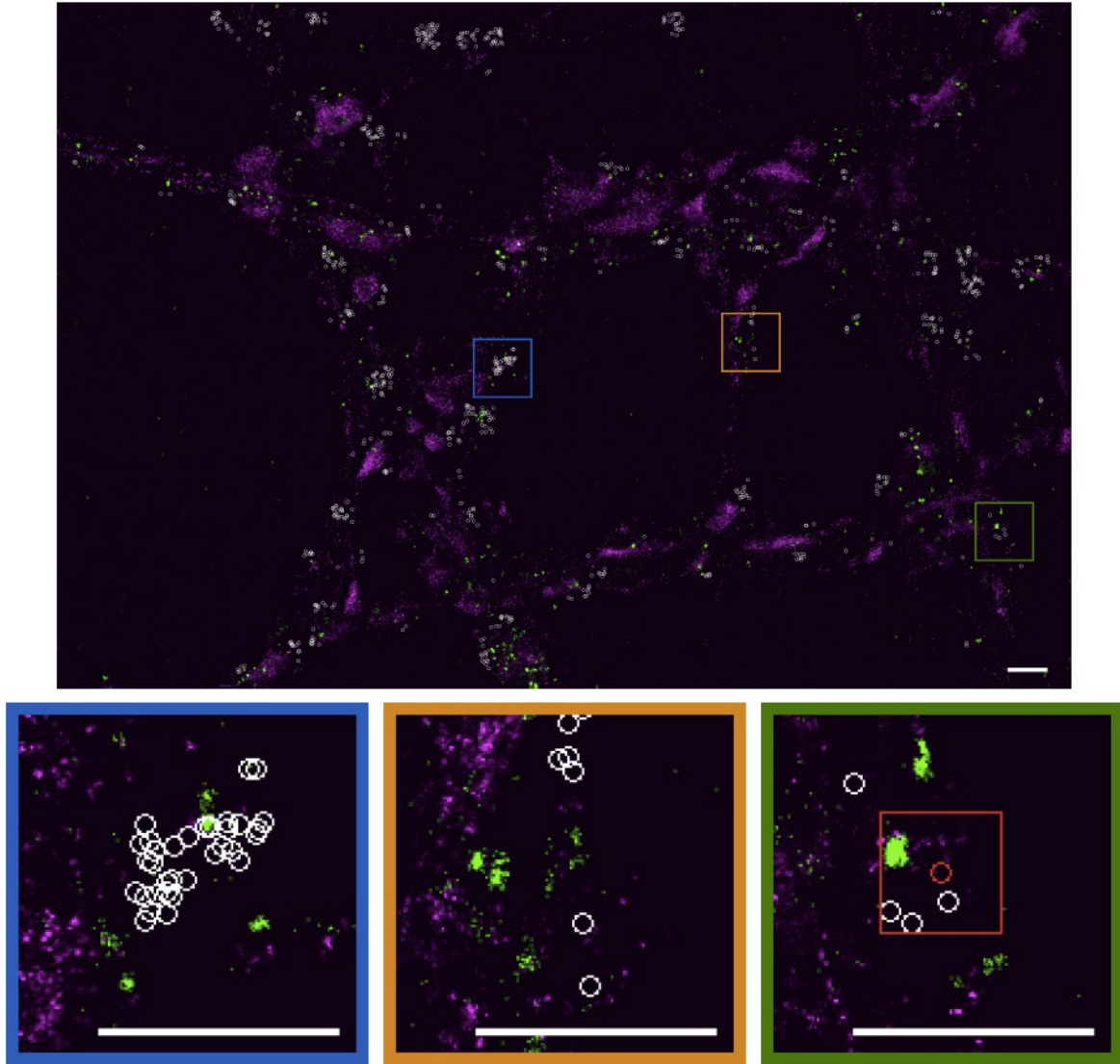


Figure 5: Colocalization of BDNF proteins and vGlut in the dSTORM images depicted in Figure 2. The colocalization regions identified by GcoPS are represented as white circles. Three zoomed-in regions are displayed at the bottom. The red rectangle represents an example of window used to find the hit shown as a red circle. The scale bars correspond to  $1\mu\text{m}$ . This figure appears in color in the electronic version of this article, and any mention of color refers to that version.

step. In fact, GcoPS is not sensitive to the presence of spurious isolated spots, because these ones are typically very small objects that are negligible in volume with respect to the whole detected random set. This contrasts with point-based methods for which each spurious point counts as much as any other detected object in the cell and falsely influences the statistical analysis. As a consequence, any segmentation algorithm can be used if it provides a biologically reasonable segmentation of the tagged molecules. Our simulation study actually confirms that GcoPS is fairly robust to the choice of segmentation algorithm parameters.

For the practical implementation of GcoPS, it is important to determine the ratio between the size of the tested window with respect to the size and the number of objects in the window. In theory, this ratio should be as large as possible so that the GcoPS colocalization score  $T_n$  is distributed as a standard Gaussian law, see Proposition 1. The control of the convergence to the Gaussian distribution, or rather the absence of control of this convergence, is a common issue in almost all testing procedures. Nonetheless, when the objects are very large with respect to the size of the windows, as in the rightmost plot in the middle row of Figure 3, GcoPS still behaves satisfyingly, proving that it is very robust to the detection of colocalization in small sub-windows of a real image. On the other hand, GcoPS (as well as the other competitive methods) also assume stationarity of the distribution of the objects inside the tested window. This hypothesis is more easily acceptable in small windows than in large windows, as illustrated in the real dataset analyzed in Section 4.2. This remark confirms the importance to use a procedure that remains effective in small windows, as GcoPS. For a safe decision, we finally recommend to use GcoPS in windows that are at least five times larger than the average size of the objects. This guarantees that a minimal fluorescence information is available to assess colocalization, while allowing to consider small sub-windows.

## Acknowledgements

We thank Jean Salamero, Markus Sauer, Soeren Doose, Sarah Aufmolk, Perrine Paul-Gilloteaux and Fabrice Cordelières for assistance with experiments and for helpful insight in the preparation of the manuscript.

## A Proof of Proposition 1

Since  $\Gamma_1$  and  $\Gamma_2$  are independent  $\mathbb{E}(\hat{D}_n) = 0$ , and by stationarity of both random sets

$$\text{Var}(\hat{D}_n) = n^{-2} \mathbb{E} \left( \sum_{x \in \Omega_n} \mathbf{1}_{\Gamma_1}(x) \mathbf{1}_{\Gamma_2}(x) - |\Omega_n|^{-1} \sum_{x \in \Omega_n} \mathbf{1}_{\Gamma_1}(x) \sum_{x \in \Omega_n} \mathbf{1}_{\Gamma_2}(x) \right)^2 = V_1 + V_2 + V_3,$$

where

$$\begin{aligned} V_1 &= n^{-2} \sum_{x \in \Omega_n} \sum_{y \in \Omega_n} C_1(x-y) C_2(x-y), \\ V_2 &= -2n^{-3} \sum_{x \in \Omega_n} \left( \sum_{y \in \Omega_n} C_1(x-y) \right) \left( \sum_{y \in \Omega_n} C_2(x-y) \right), \\ V_3 &= n^{-4} \sum_{x \in \Omega_n} \sum_{y \in \Omega_n} C_1(x-y) \sum_{x \in \Omega_n} \sum_{y \in \Omega_n} C_2(x-y). \end{aligned}$$

Since  $\Gamma_1$  and  $\Gamma_2$  are  $R$ -dependent,  $C_1$  and  $C_2$  are summable, implying  $V_1 = O(n^{-1})$ ,  $V_2 = O(n^{-2})$  and  $V_3 = O(n^{-2})$ , as  $n \rightarrow \infty$ . Therefore

$$\text{Var}(\hat{D}_n) \sim V_1 \sim n^{-1} \sum_{h \in \mathbb{Z}^d, \|h\| \leq R} C_1(h) C_2(h), \text{ as } n \rightarrow \infty.$$

Concerning the asymptotic normality of  $\hat{D}_n$ , let us first consider  $\hat{p}_{12}$ . We have

$$n(\hat{p}_{12} - p_{12}) = \sum_{x \in \Omega_n} X_x,$$

where  $X_x = \mathbf{1}_{\Gamma_1 \cap \Gamma_2}(x) - p_{12}$ .  $(X_x)_{x \in \mathbb{Z}^d}$  is a real valued stationary centered random field on  $\mathbb{Z}^d$ , which inherits the  $R$ -dependency from  $\Gamma_1$  and  $\Gamma_2$  and admits moments of any order. A central limit theorem then applies, see for instance [Bolthausen \(1982\)](#) where all mixing conditions are verified by the  $R$ -dependent assumption. We get

$$n^{-1/2} \sum_{x \in \Omega_n} X_x \xrightarrow{d} \mathcal{N}(0, \sigma^2)$$

as  $n \rightarrow \infty$ , where

$$\sigma^2 = \sum_{h \in \mathbb{Z}^d} \mathbb{E}(X_o X_h) = \sum_{h \in \mathbb{Z}^d, \|h\| \leq R} C_{12}(h),$$

and  $C_{12}$  denotes the autocovariance function of the random set  $\Gamma_1 \cap \Gamma_2$ . This gives us the asymptotic normality of  $n^{1/2}(\hat{p}_{12} - p_{12})$ . Thanks to the Cramer-Wold device, we can prove similarly the joint asymptotic normality of  $n^{1/2}(\hat{p}_{12} - p_{12})$ ,  $n^{1/2}(\hat{p}_1 - p_1)$  and  $n^{1/2}(\hat{p}_2 - p_2)$ . The  $\Delta$ -method then provides the asymptotic normality of  $n^{1/2}\hat{D}_n$ . The asymptotic variance of this term is deduced from our preliminary computations and we obtain that

$$\sqrt{n} \frac{\hat{D}_n}{\sqrt{\sum_{h \in \mathbb{Z}^d, \|h\| \leq R} C_1(h)C_2(h)}} \xrightarrow{d} \mathcal{N}(0, 1),$$

as  $n \rightarrow \infty$ . Replacing  $C_1(h)$  and  $C_2(h)$  by consistent estimators does not change the result, by application of Slutsky's lemma, since the sum above is finite.

## B Evaluation on synthetic data sets: details

This section is a detailed version of Section 3 of the main manuscript. The objective is to evaluate the performances of GcoPS, in comparison to the competitive Costes method (Costes et al., 2004) and the object-based method of Lagache et al. (2015), in various adverse situations. As a first comparison, Figure S6 depicts the workflow for each testing method, starting from the same raw image. For implementation, we use JACoP plugin (Bolte and Cordelieres, 2006) on ImageJ (Schneider et al., 2012) to apply the Costes method: i) in the randomization step,  $n = 1000$  replications are considered; ii) we choose blocks of pixels with a size corresponding to the PSF (point spread function) for simulated images, as advised in Costes et al. (2004), and corresponding to the average size of the objects for segmented images. For the Lagache method, we use the colocalization studio in Icy (de Chaumont et al., 2012). Moreover, we recall that we have implemented GcoPS within the Icy software, where it is available as a downloadable module (more details at <http://icy.bioimageanalysis.org/plugin/GcoPS>).

### B.1 Time computation

Table 1 gives the CPU time for the three methods applied to 2D, 2D+t and 3D images, depending on the number of objects detected after segmentation. As expected, the Costes procedure, which is not an object-based method, is not sensitive to the number of objects. However, it is by far the slowest method because of the Monte Carlo step. On the contrary, the object-based method of Lagache et al. (2015) strongly depends on the number of objects

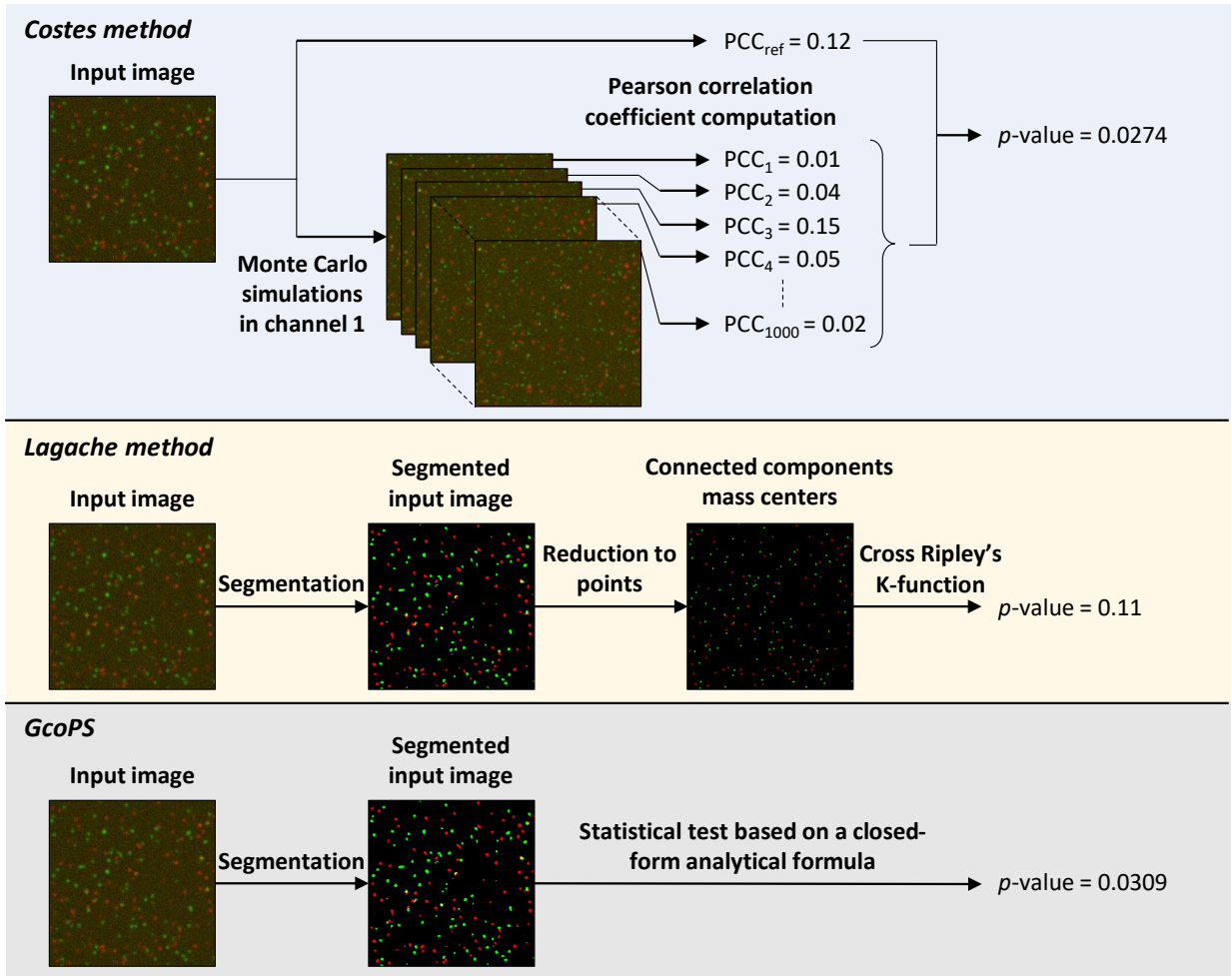


Figure S6: Schematic workflow for the intensity-based method of Costes et al. (2004), the object-based method of Lagache et al. (2015) and GcoPS, when implementing a colocalization testing procedure from the same raw image.

and can therefore be quite slow if this number is large, which is typically the case in 3D. In contrast, GcoPS is very fast whatever the situation is and is not sensitive to the number of objects. The CPU time of GcoPS is of course minimal when implemented on C++ and is slightly less optimal with the Icy plugin (based on Java), nevertheless keeping much faster than the two alternative methods.

	<b>2D image</b> 256 × 256 50 objects	<b>2D image</b> 256 × 256 200 objects	<b>2D image</b> 256 × 256 3500 objects	<b>2D+time image</b> 256 × 256 × 1000 100 objects	<b>3D image</b> 256 × 256 × 60 1000 objects	<b>3D image</b> 256 × 256 × 60 2000 objects
<b>Costes et al. (2004)</b> ImageJ plugin	6.1 sec	6.2 sec	6.1 sec	38 min 20 sec	3 min 3 sec	3 min 10 sec
<b>Lagache et al. (2015)</b> Icy plugin	1 sec	1.96 sec	12.38 sec	12 min 39 sec	25 sec	60 sec
<b>GcoPS</b> C++ code	<b>0.18 sec</b>	<b>0.2 sec</b>	<b>0.19 sec</b>	<b>29.5 sec</b>	<b>10 sec</b>	<b>9.8 sec</b>
<b>GcoPS</b> Icy plugin	<b>0.77 s</b>	<b>0.86 sec</b>	<b>0.82 sec</b>	<b>2 min 50 sec</b>	<b>22 sec</b>	<b>21 sec</b>

Table 1: Comparison of computation time of the intensity-based method of [Costes et al. \(2004\)](#), the object-based method of [Lagache et al. \(2015\)](#) and GcoPS, when applied to 2D, 2D+time and 3D images.

## B.2 Evaluation on simulated 2D images

We evaluate the sensitivity of the methods on synthetic images generated by the simulator described in [Lagache et al. \(2015\)](#). This simulator consists in a first step to generate randomly distributed particles (say the red channel), and in a second step to simulate a proportion of green particles nearby red particles while the rest of green particles are drawn randomly and independently. Note that the following figures appear in color in the electronic version of this article, and any mention of color refers to that version. Three scenarios are considered: i) without noise, ii) with noise and iii) with noise and a spatial shift of three pixels between colocalized particles (a 3 pixels shift is more than enough to account for a possible spatial shift due to the experimental device). In each of these scenarios, the two channels were simulated with a proportion of forced neighbors of 0% (no colocalization), 2.5% and 5%. In each situation, 1000 pairs of images were generated to evaluate the sensitivity of the three tested methods.

Figure [S7](#) compares the results of GcoPS, the object-based method of [Lagache et al. \(2015\)](#) and the intensity-based method of [Costes et al. \(2004\)](#) for the first scenario (no noise, no shift), by reporting the proportion of  $p$ -values lower than 0.05, along with the empirical distribution function (edf) of the  $p$ -values. Recall that a perfect testing procedure would

result in an edf equal to the first diagonal in absence of colocalization and in an edf which is uniformly equal to 1 in presence of colocalization. Figure S7 reveals that the object-based method is not sufficiently sensitive (less than 35% of images have a  $p$ -value inferior to 0.05 with 5% forced neighbors against more than 90% for GcoPS). The Costes method is in turn too sensitive in absence of colocalization (about 18% of images without colocalization have a  $p$ -value lower than 0.05), which leads to too many false positive decisions. These observations are confirmed by the simulations carried out in the other two scenarios, see Figures S8 and S9, where the power of GcoPS is clearly superior to the other methods (twice more images have a  $p$ -value lower than 0.05 with 5% forced neighbors in presence of noise and/or shift). Finally, Figure S10 displays an unbalanced situation where the number of objects in one channel is 4 times superior to the number of objects than in the other channel. The results confirm the previous conclusions.

### B.3 Sensitivity to image segmentation

To evaluate the influence of the segmentation for the different methods, we consider the same simulated images with noise and shift as in the previous section but with four different thresholds of segmentation. We then apply the same methods as described in the previous section. As a reference, we also include the segmentation obtained with the ATLAS spot detection method (Basset et al., 2015), which is the segmentation method used in all experiments presented in the paper. An example of segmented image is given in Figure S11. As a result, see Figures S12-S14, the intensity-based method of Costes et al. (2004) is not much affected by the pre-processing and is even slightly more sensitive than GcoPS when the proportion of forced neighbors is 2.5% and 5%. However, this method clearly leads to too many false positive decisions when there is no colocalization, confirming a conclusion made in the previous section. The object-based method of Lagache et al. (2015) is in turn clearly affected by over-segmentation, in which case it completely fails to detect colocalization. GcoPS is also less efficient when the segmentation is not well processed, but the results are overall still satisfying. In particular GcoPS is very robust to pre-processing for images without colocalization, which is a safe guaranty against false positive decisions.

### B.4 Sensitivity to the shape and scale of objects

To evaluate the sensitivity to the shape and the size (or scale) of objects, we have simulated Gaussian level sets with a correlation between the two channels equal to 0 (*i.e.*, no colocalization), 0.1 (slight colocalization) and 0.3 (stronger colocalization) approximately. This

method of simulation is detailed in Section C. It allows to generate objects that exhibit non-regular shapes (different from balls), with a typical scale that can be easily controlled. When the objects are small (not shown in our figures), the images are quite similar to the images generated in Section B.2, or in other words the objects are fairly assimilable to small balls, and the methods show similar efficiency as described above. In presence of non regular objects, as shown in Figure S15, the intensity-based method of Costes et al. (2004) is once again too sensitive for colocalization while the object-based method of Lagache et al. (2015) is not sufficiently sensitive, especially when the correlation between the two channels is 0.1. In contrast, the performance of GcoPS is not disrupted by the shape of objects. In presence of larger objects, as depicted in Figure S16, the conclusions are similar. Finally, in the extreme case of very large objects, see Figure S17, the object-based method, that reduces each object to a single point, completely fails to detect colocalization, which is easily explained by the dramatic loss of information induced by this reduction. In this case, the Costes method is far too sensitive (about 25% of false positive decisions in absence of colocalization), while GcoPS still performs well, though being a bit too sensitive when there is no colocalization. The robustness of GcoPS in presence of large objects shows that this method can be applied to small windows in the image, where the scaling makes objects larger, hence opening the possibility to effectively localize the detection of colocalization.

## B.5 Performance in presence of a different optical resolution in each image

To generate images with a different optical resolution, we have simulated Gaussian level sets where the scale parameter ruling the typical size of objects is different in each image. The details are given in Section C. The correlation between the two images is as in the previous section  $\rho = 0$ ,  $\rho = 0.1$  or  $\rho = 0.3$ .

Figures S18 and S19 show situations with a difference in optical resolution (moderate and strong respectively). The results demonstrate that the object-based method of Lagache et al. (2015) is clearly outperformed by the other methods in presence of a difference of optical resolution. The intensity-based method of Costes et al. (2004) is more robust but GcoPS exhibits better efficiency. This proves that GcoPS is able to process efficiently images for which a different microscopy technique is used for detecting each type of molecules.

## B.6 Evaluation on simulated 3D images

We have performed simulations of 3D objects using Gaussian level sets (see Section C for details) to generate channels with a correlation equal to 0, 0.1 and 0.3. The results are displayed in Figure S20. The object-based method of Lagache et al. (2015) shows very unsatisfying results when there is no colocalization. The intensity-based method of Costes et al. (2004) is in turn even more sensitive to colocalization in 3D than it is in 2D, leading to too many false positive conclusions when the two images are independent. The results obtained with GcoPS on 3D images are in line with the results obtained with 2D images and demonstrate the better overall performance of this method. Note finally that we have also performed complementary simulations in 3D, not displayed here, to assess the robustness of GcoPS against shape anisotropy (e.g. elongated shapes in 3D) and/or a low density of particles. The results demonstrate that the performance of GcoPS is not altered.

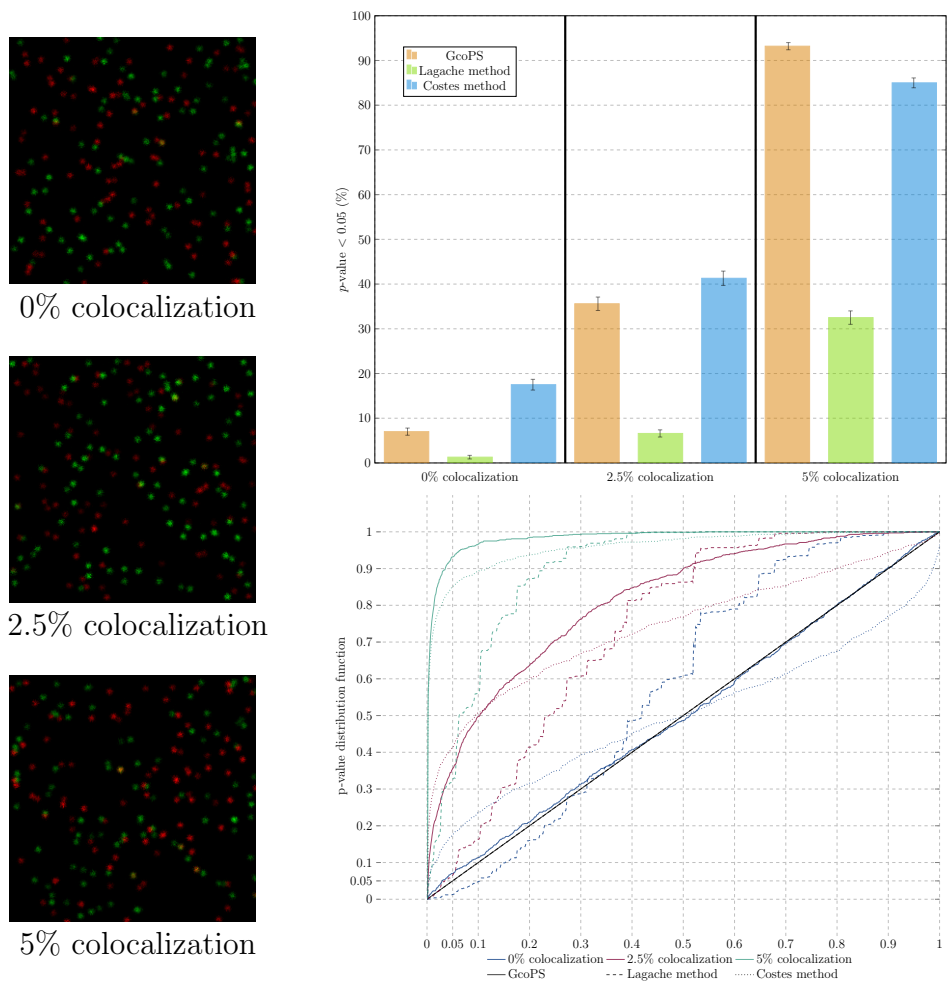
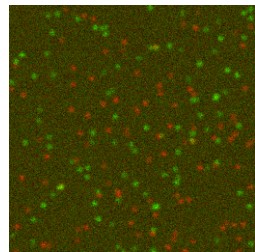
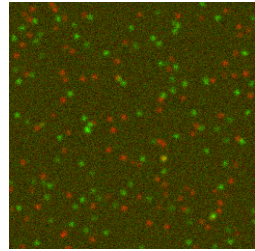


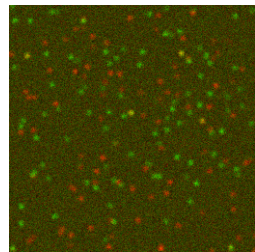
Figure S7: Evaluation of GcoPS on 2D simulated images. Top right: proportion of  $p$ -values lower than 0.05 obtained with GcoPS, the object-based method of Lagache et al. (2015) and the intensity-based method of Costes et al. (2004) over 1000 simulated images without noise and without shift for 0%, 2.5% and 5% forced neighbors. The confidence intervals at the top of each bar represent one standard deviation over all 1000 simulations. Bottom right: empirical distribution functions of  $p$ -values. Left: an example of simulated images.



0% colocalization



2.5% colocalization



5% colocalization

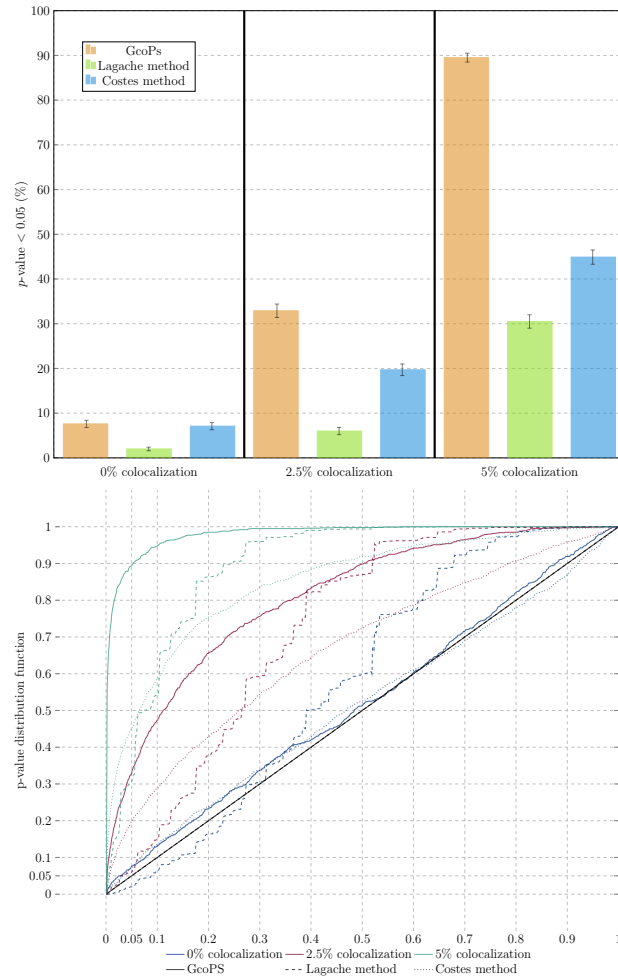
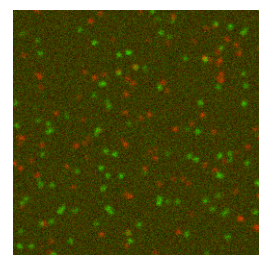
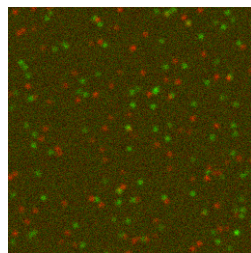


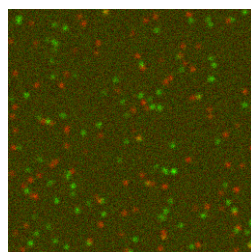
Figure S8: Evaluation of GcoPS on 2D simulated images with noise. Same plots as in Figure S7 except that the simulated images are corrupted with noise.



0% colocalization



2.5% colocalization



5% colocalization

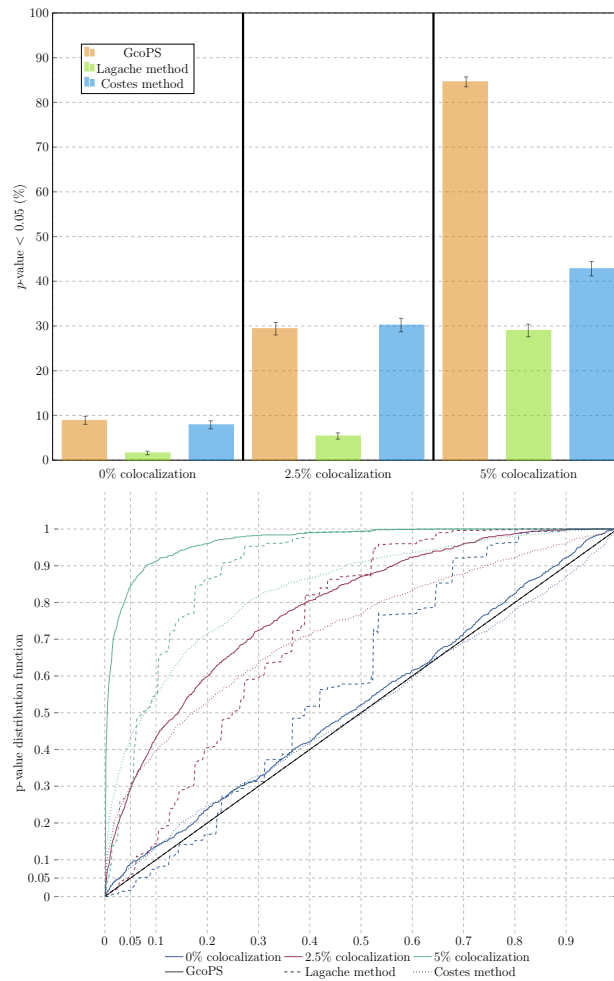
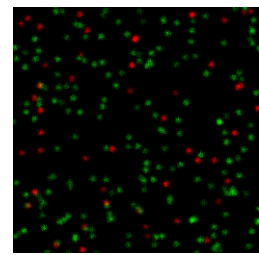
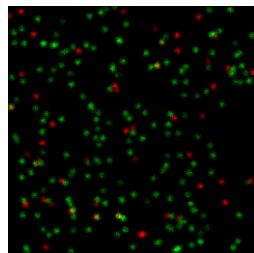


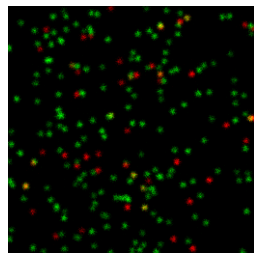
Figure S9: Evaluation of GcoPS on 2D simulated images with noise. Same plots as in Figure S7 except that the simulated images are corrupted with noise and a shift of three pixels is applied between the two channels.



0% colocalization



2.5% colocalization



5% colocalization

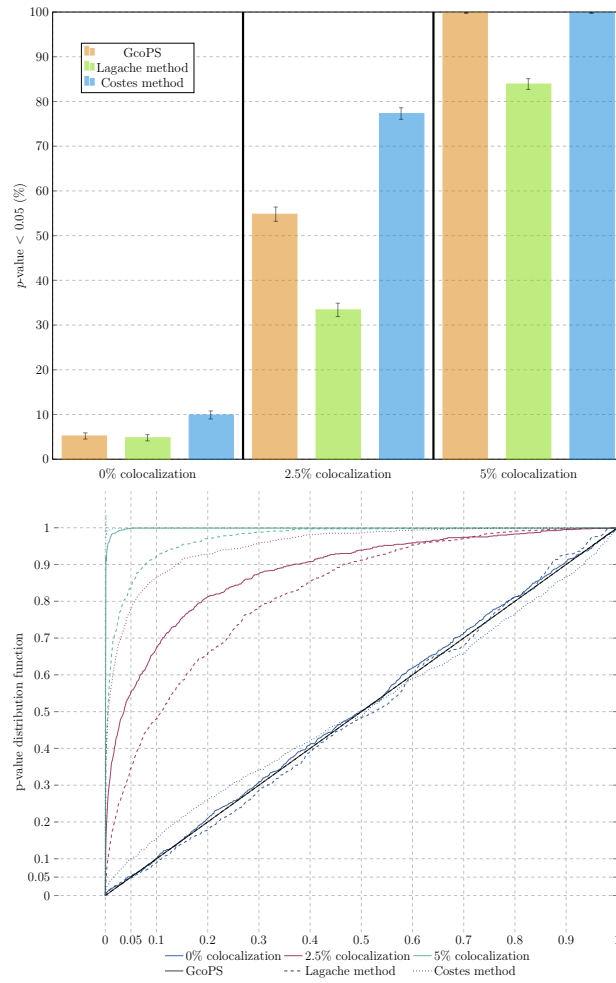


Figure S10: Evaluation of GcoPS on 2D simulated images with noise. Same plots as in Figure S7 except that the green channel shows 4 times more objects than the red channel.

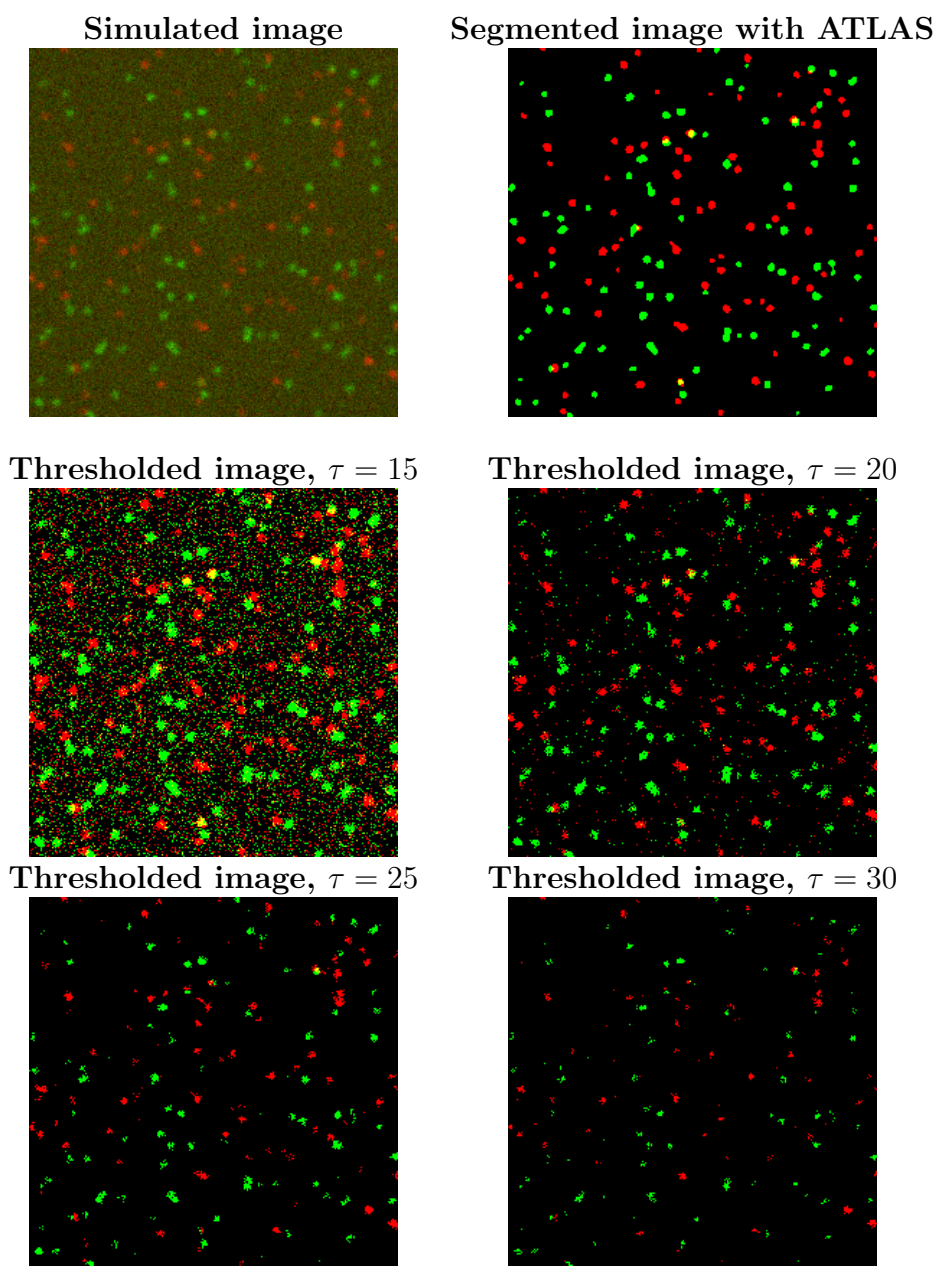


Figure S11: Sensitivity to segmentation. Example of a simulated image with noise and shift and the corresponding segmentations with ATLAS (Basset et al., 2015) and a threshold  $\tau$  ranging from 15 to 30.

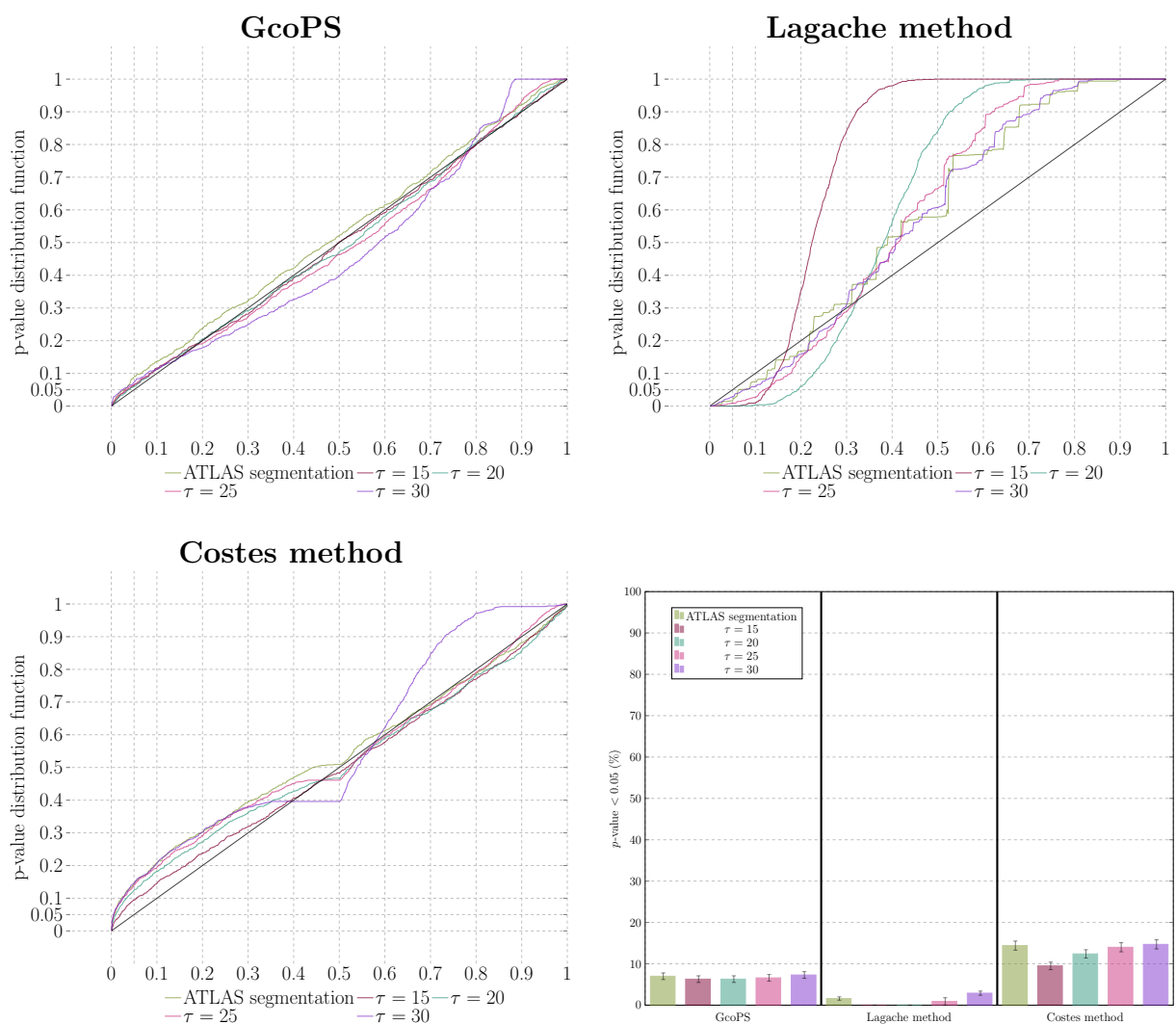


Figure S12: Sensitivity to segmentation. Proportion of  $p$ -values lower than 0.05 (bottom right) and empirical distribution functions of  $p$ -values obtained with (from top left to bottom left) GcoPS, the object-based method of [Lagache et al. \(2015\)](#) and the intensity-based method of [Costes et al. \(2004\)](#) over 1000 simulated images with noise and shift, segmented with ATLAS ([Basset et al., 2015](#)) or a threshold  $\tau$  ranging from 15 to 30, when there is no colocalization.

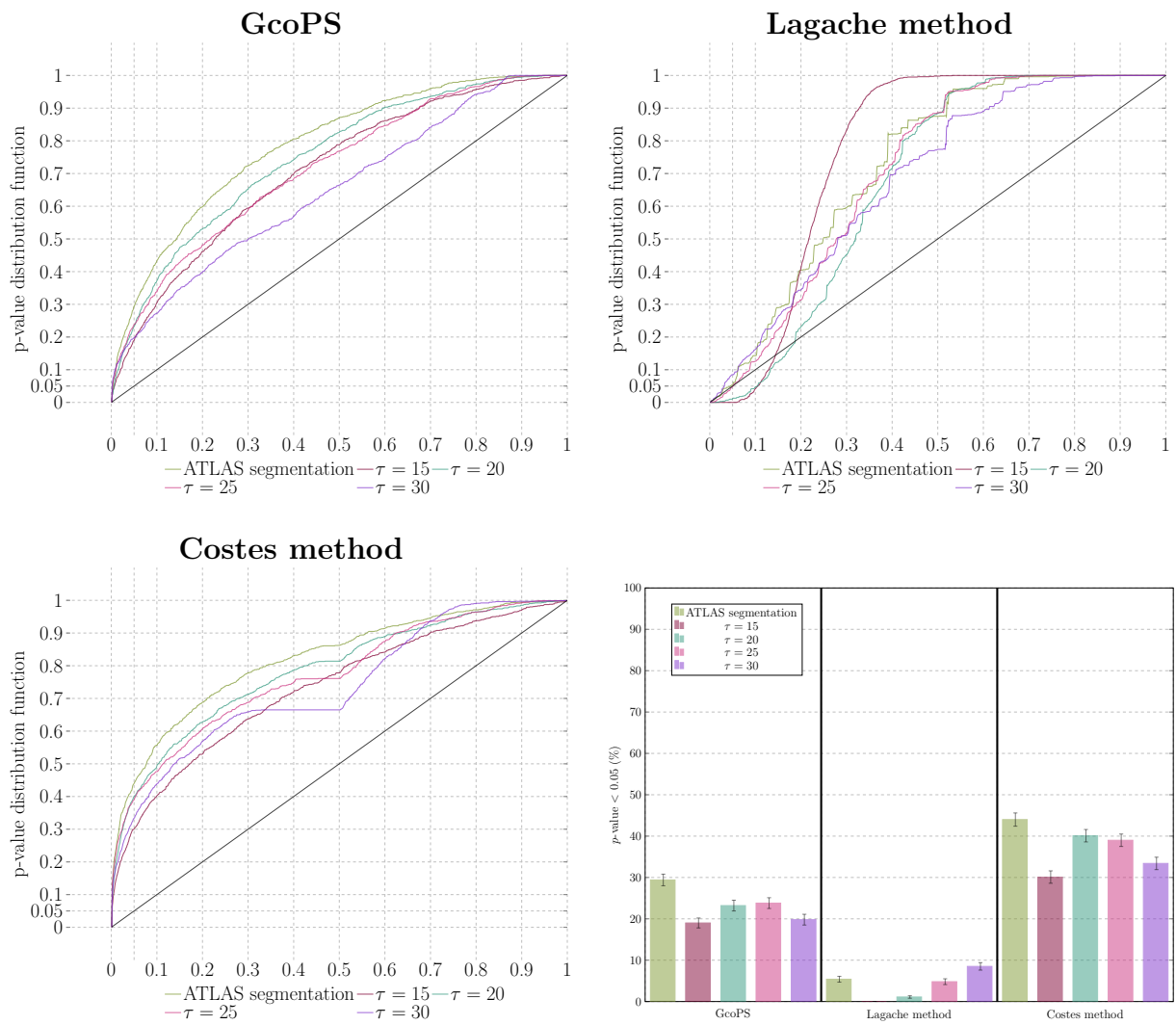


Figure S13: Sensitivity to segmentation. Same plots as in Figure S12 but for 2.5% forced neighbors.

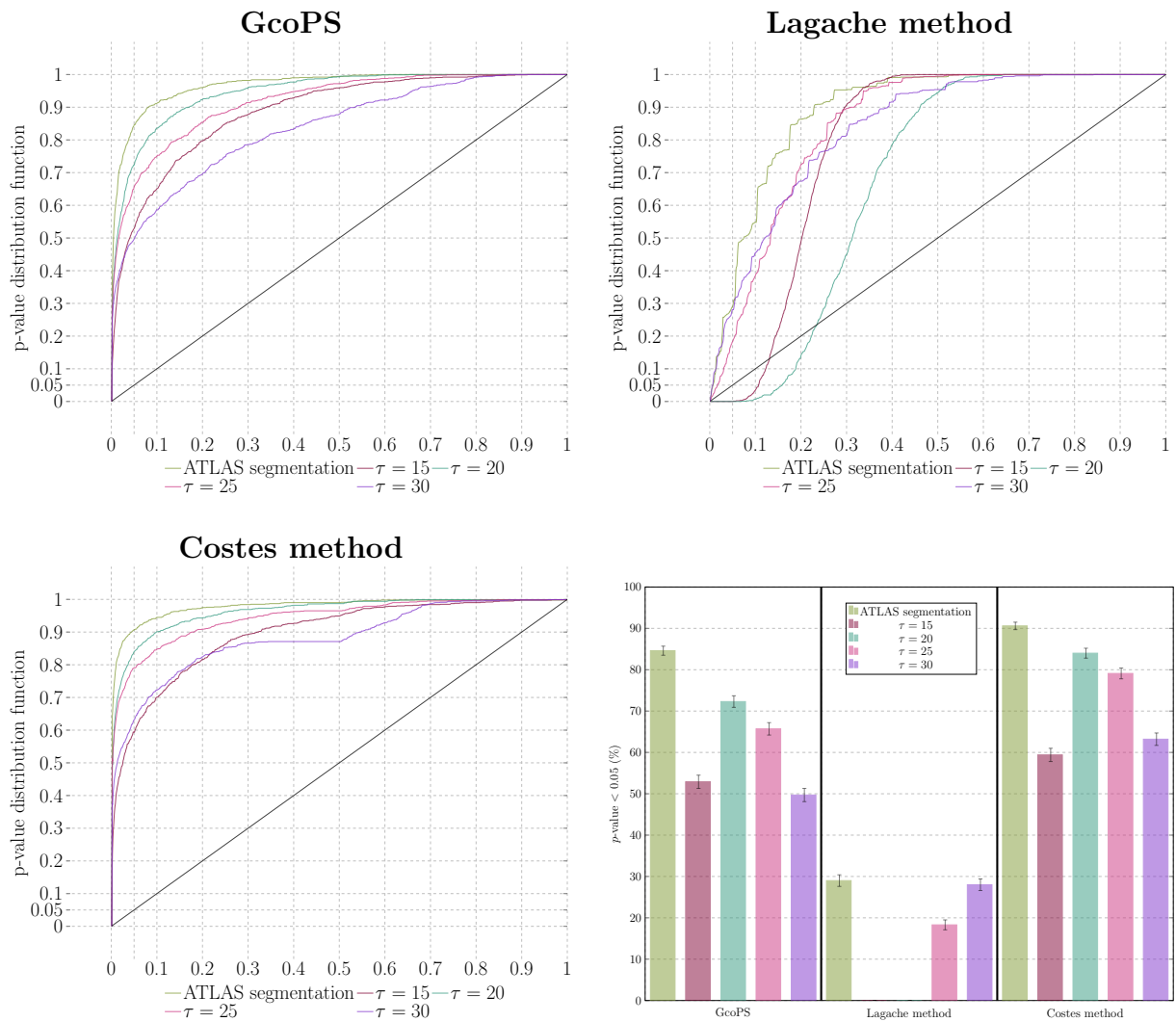


Figure S14: Sensitivity to segmentation. Same plots as in Figure S12 but for 5% forced neighbors.

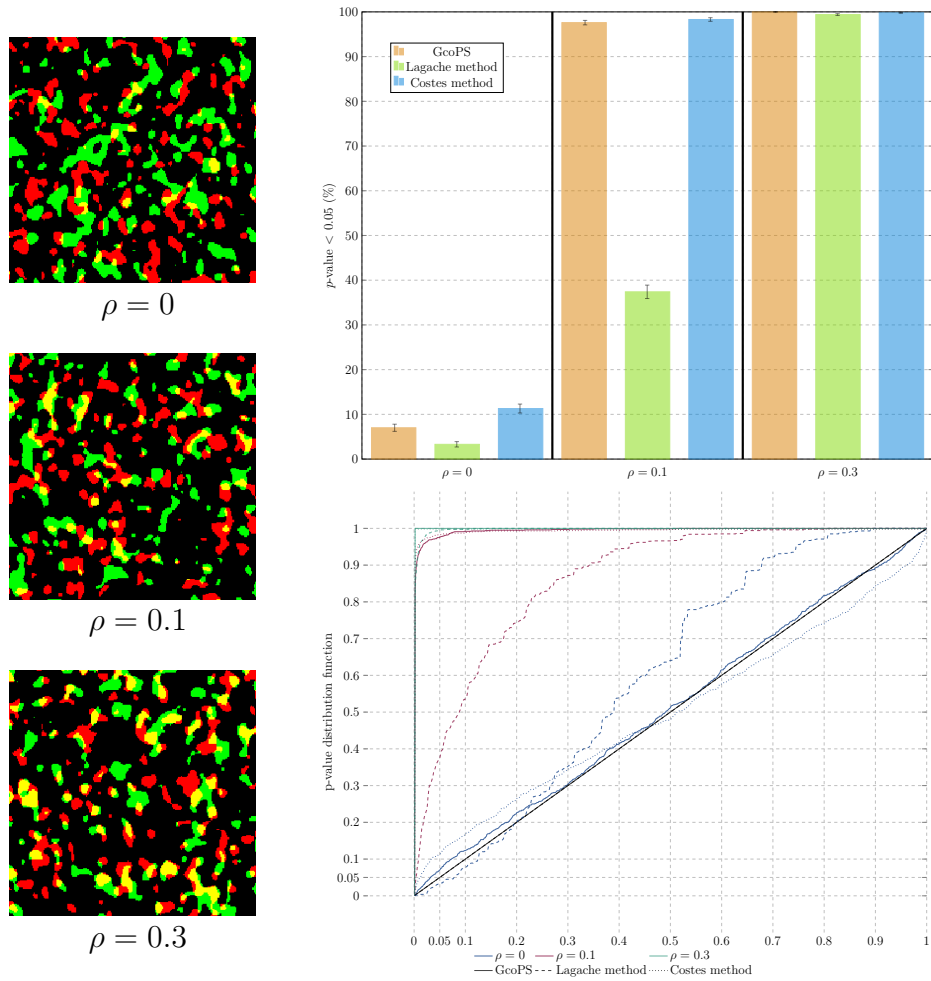
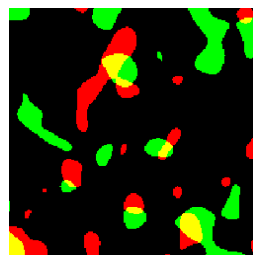
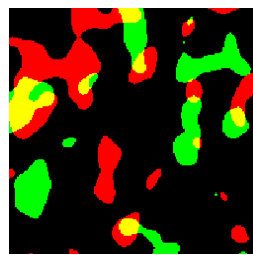


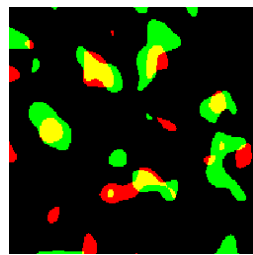
Figure S15: Sensitivity to the shape and scale of objects. Proportion of  $p$ -values lower than 0.05 (top right) and empirical distribution functions (bottom right) of  $p$ -values obtained with GcoPS, the object-based method of [Lagache et al. \(2015\)](#) and the intensity-based method of [Costes et al. \(2004\)](#) over 1000 simulated images obtained via Gaussian level sets with a correlation equal to 0, 0.1 and 0.3 between the two channels, resulting in non regularly shaped objects. An example of simulated images is shown at the left of the plot.



$\rho = 0$



$\rho = 0.1$



$\rho = 0.3$

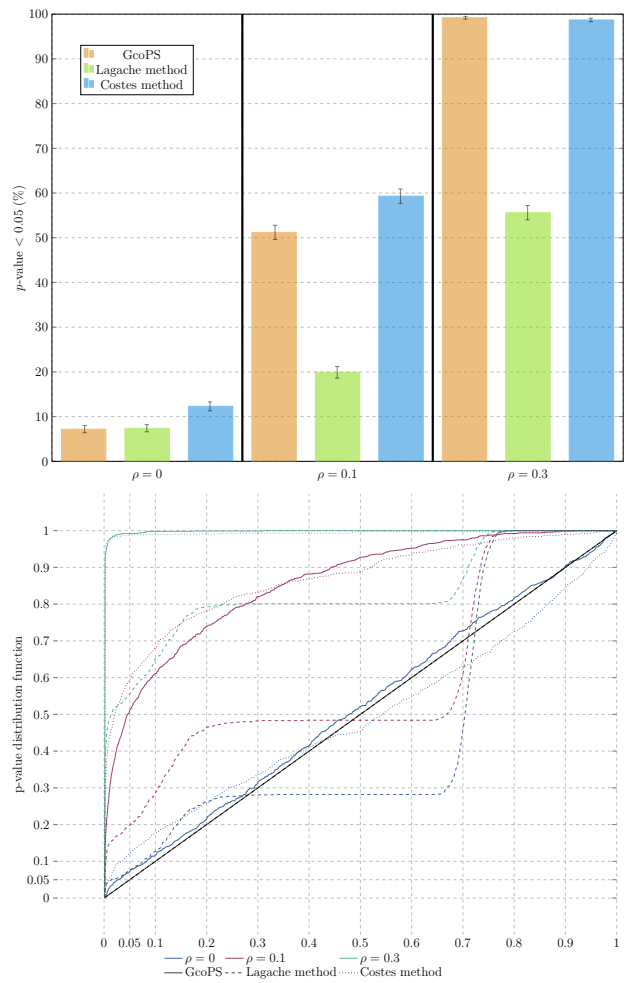


Figure S16: Sensitivity to the shape and scale of objects. Same plots as in Figure S15 but the objects are larger.

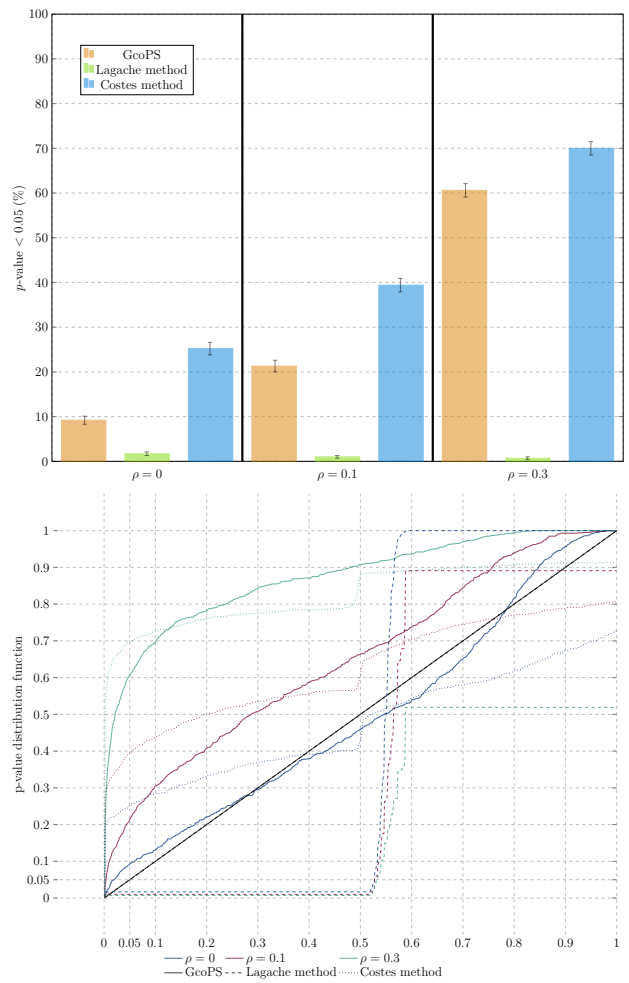
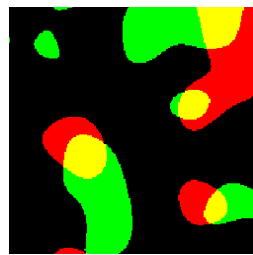
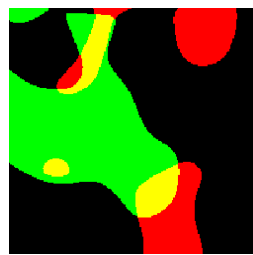
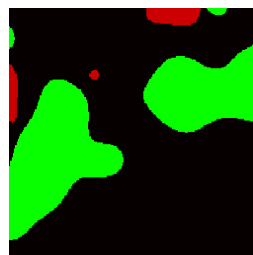


Figure S17: Sensitivity to the shape and scale of objects. Same plots as in Figure S15 but the objects are even larger than in Figure S16.

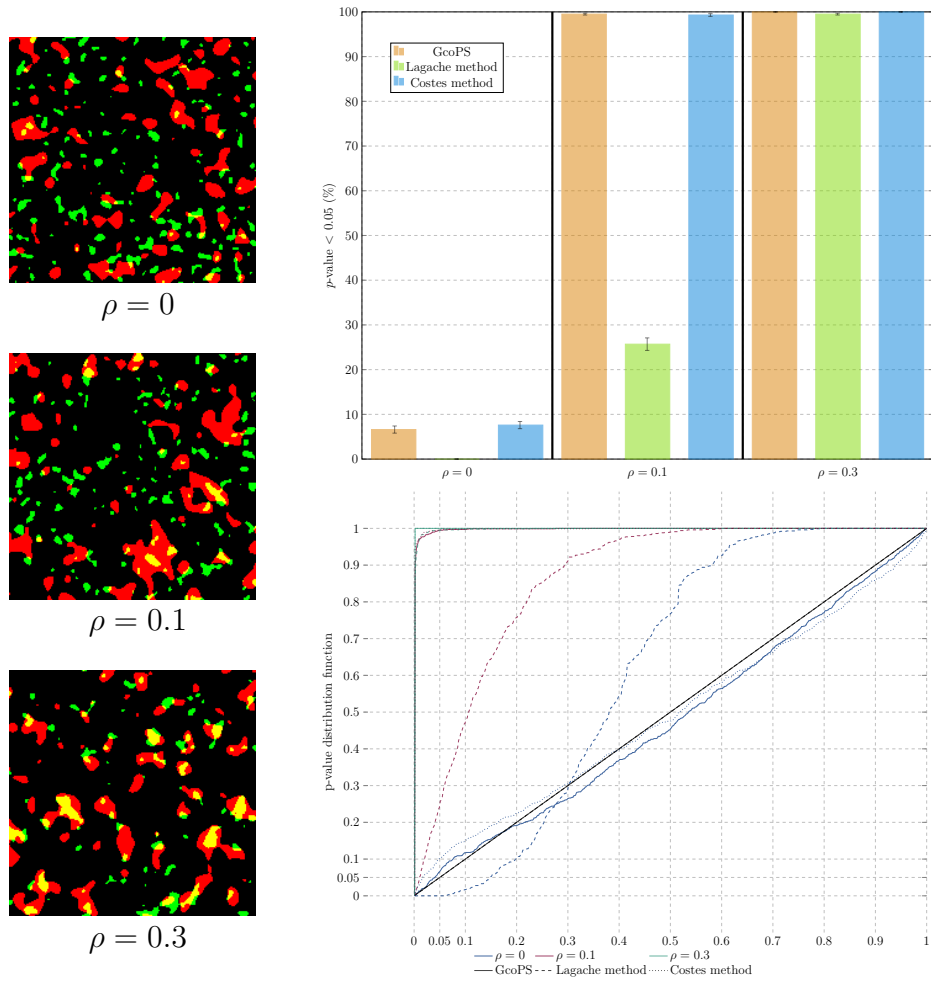
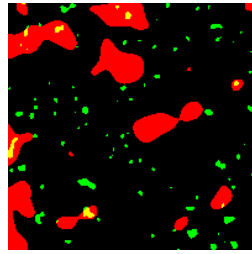
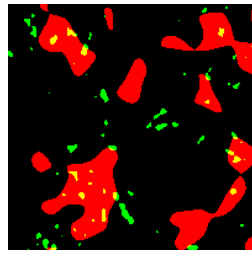


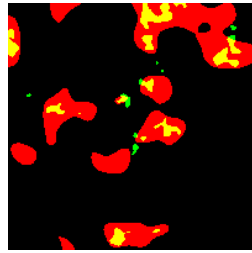
Figure S18: Sensitivity to the resolutions in each channel. Proportion of  $p$ -values lower than 0.05 (top right) and empirical distribution functions (bottom right) of  $p$ -values obtained with GcoPS, the object-based method of Lagache et al. (2015) and the intensity-based method of Costes et al. (2004) over 1000 simulated images obtained via Gaussian level sets with a correlation equal to 0, 0.1 and 0.3 between the two channels, where the resolution is different in each channel. An example of simulated images is shown at the left of the plot.



$\rho = 0$



$\rho = 0.1$



$\rho = 0.3$

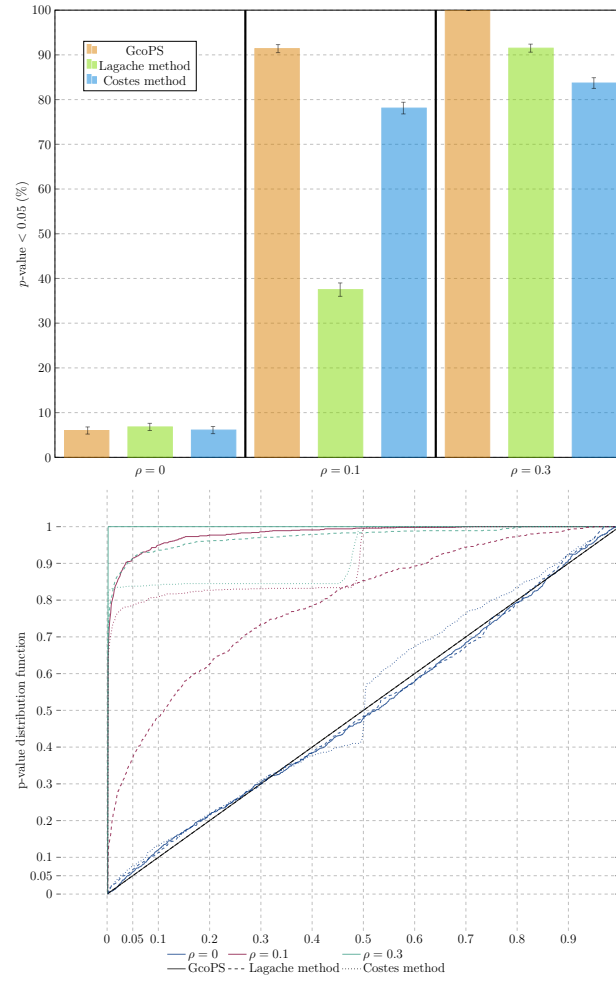


Figure S19: Sensitivity to the resolutions in each channel. Same plots as in Figure S18 but the difference in resolution is larger.

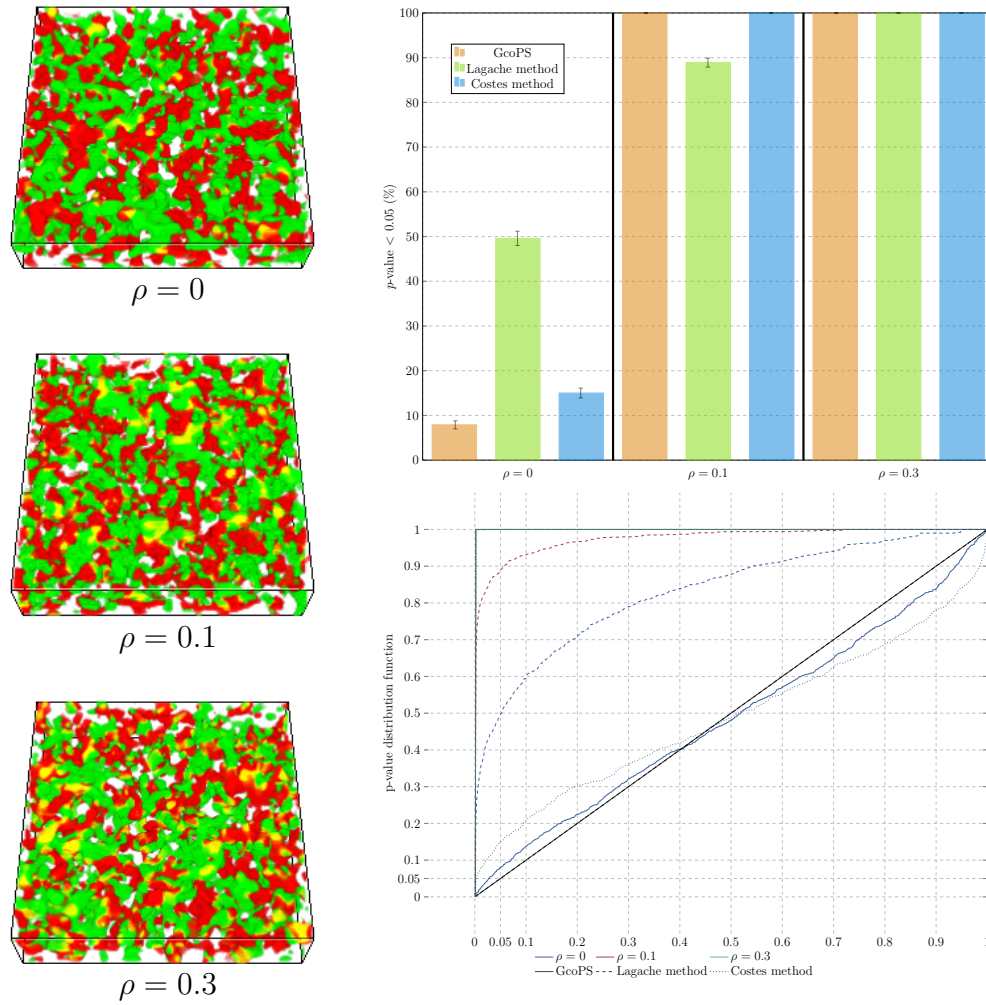


Figure S20: Evaluation on 3D images. Proportion of  $p$ -values lower than 0.05 (top right) and empirical distribution functions (bottom right) of  $p$ -values obtained with GcoPS, the object-based method of [Lagache et al. \(2015\)](#) and the intensity-based method of [Costes et al. \(2004\)](#) over 1000 simulated images obtained via 3D Gaussian level sets with a correlation equal to 0, 0.1 and 0.3 between the two channels. An example of simulated images is shown at the left of the plot.

## C Simulations by Gaussian level sets

Let  $X, Y$  and  $\epsilon$  be three independent Gaussian random fields in  $\mathbb{R}^d$  with isotropic covariance function

$$C(r) = \sigma^2 e^{-r^2/\alpha^2}, \quad r \geq 0,$$

where  $r$  denotes the radial distance between two points of the field,  $\sigma^2$  is the variance and  $\alpha > 0$  is referred to as the scale parameter. These parameters are denoted by  $\sigma_X^2, \sigma_Y^2, \sigma_\epsilon^2$  and  $\alpha_X, \alpha_Y, \alpha_\epsilon$ , for  $X, Y$  and  $\epsilon$  respectively. Henceforth, for  $\rho_0 \in [-1, 1]$ , we set

$$\sigma_X^2 = \sigma_Y^2 =: \sigma_0^2 \quad \text{and} \quad \sigma_\epsilon^2 = \frac{\rho_0}{1 - \rho_0} \sigma_0^2.$$

We define the random fields

$$U = X + \epsilon \quad \text{and} \quad V = Y + \epsilon.$$

Note that  $U$  and  $V$  are Gaussian random fields with common variance  $\sigma^2 = \sigma_0^2/(1 - \rho_0)$  and that  $U$  and  $V$  are correlated with correlation  $\rho_0$ . We finally consider the random sets induced by the level sets of  $U$  and  $V$ , for  $\tau_1 > 0$  and  $\tau_2 > 0$ ,

$$\Gamma_1 = \{U > \tau_1 \sigma\} \quad \text{and} \quad \Gamma_2 = \{V > \tau_2 \sigma\}.$$

We easily get the following properties :

- The random set  $\Gamma_1$ , respectively  $\Gamma_2$ , has a coverage rate equal to  $p_1 := \mathbb{P}(o \in \Gamma_1) = 1 - \Phi(\tau_1)$  (for any  $o \in \mathbb{R}^d$ ), respectively  $p_2 := 1 - \Phi(\tau_2)$ , where  $\Phi$  denotes the cumulative distribution function of a standard normal law. Recall that this coverage rate represents the proportion of 1's, in average, generated by the binary field  $\Gamma_1$  in a given domain.
- The random sets  $\Gamma_1$  and  $\Gamma_2$  are correlated with correlation

$$\rho = \left( \int_{\tau_1}^{\infty} \int_{\tau_2}^{\infty} f(u, v) du dv - p_1 p_2 \right) / \sqrt{p_1(1 - p_1)p_2(1 - p_2)},$$

where  $f$  denotes the marginal probability density function of  $(U, V)$  that is the density of a bivariate centered Gaussian random variable with covariance matrix  $\sigma^2 \begin{bmatrix} 1 & \rho_0 \\ \rho_0 & 1 \end{bmatrix}$ .

In order to generate two correlated binary images containing random spots in a given domain, say  $\Omega_n$ , we therefore simulate  $\Gamma_1$  and  $\Gamma_2$  in  $\Omega_n$ . The input parameters are first the scale parameters  $\alpha_X$ ,  $\alpha_Y$  and  $\alpha_\epsilon$  that rule the size of the spots (the larger the scale parameters, the larger the spots), second the thresholds  $\tau_1$  and  $\tau_2$  that rule the density of spots in  $\Omega_n$  (see the expression of  $p_1$  and  $p_2$ ), third  $\rho_0$  and  $\sigma_0$  that along with the thresholds influence the correlation  $\rho$  between the two channels.

Given the input parameters, the simulation is straightforward. It basically amounts to simulate the Gaussian random fields  $X$ ,  $Y$  and  $\epsilon$  on  $\Omega_n$ . We use at this step the `RandomFields` package (Schlather et al., 2017) of the free available software R (R Core Team, 2017). Then the random fields  $U$  and  $V$ , and finally the binary images induced by  $\Gamma_1$  and  $\Gamma_2$ , are easily deduced.

In the simulations of Section B.4, we used as input parameters  $\sigma_0 = 1$ ,  $\tau_1 = \tau_2 = 1$ , resulting in a density of spots of  $p_1 = p_2 \approx 16\%$ , and  $\rho_0 = 0, 0.2, 0.5$  leading to an actual correlation between the two channels of  $\rho = 0, 0.1, 0.3$  approximately. The domain of simulation was  $\Omega_n = [0, 250]^2$ . As to the scale parameters (that have no impact on the values of  $p_1$ ,  $p_2$  and  $\rho$ ), we chose  $\alpha_X = \alpha_Y = \alpha_\epsilon = 8, 20, 50$  resulting in small, large or very large spots. Concerning Section B.5, the difference of optical resolution in the two images can be controlled by different scale parameters and/or thresholds parameters in the two channels. We set  $\alpha_X = 5$ ,  $\alpha_Y = \alpha_\epsilon = 10$ ,  $\tau_1 = 1.5$ ,  $\tau_2 = 1$  (moderate difference of resolution) and  $\alpha_X = 5$ ,  $\alpha_Y = \alpha_\epsilon = 20$ ,  $\tau_1 = 2$ ,  $\tau_2 = 1$  (large difference). The value of  $\rho_0$  in these simulations has been tuned to result in the same final correlation between the channels as in Section B.4, namely  $\rho = 0, 0.1$  and  $0.3$  approximately. Finally, in the 3D experiments of Section B.6, the domain of simulation is  $\Omega_n = [0, 250]^2 \times [0, 60]$  and the input parameters are exactly the same as in Section B.4 with the choice  $\alpha_X = \alpha_Y = \alpha_\epsilon = 8$ .

## D Data preparation

We refer to Andreska et al. (2014) for the description of data shown in Figure 2 of the main manuscript, that are BDNF proteins and vGlut acquired with dSTORM.

For the set of experiments shown in Figure 1, wild type RPE1 cells were grown in Dulbecco’s Modified Eagle Medium: Nutrient Mixture F-12 (DMEM/F12) supplemented with 10% (vol/vol) FCS, in 6 well plates. RPE1 cells were transiently transfected with plasmids coding for Langerin-YFP and Langerin-mCherry or Rab11a-GFP and Langerin-mCherry using the following protocol: 2  $\mu\text{g}$  of each DNAs, completed to 100  $\mu\text{L}$  with DMEM/F12 (FCS free) were incubated for 5 min at room temperature. 6  $\mu\text{L}$  of X-tremeGENE 9 DNA

Transfection Reagent (Roche) completed to 100  $\mu\text{L}$  with DMEM/F12 (FCS free), were added to the mix and incubated for further 15 min at room temperature. The transfection mix was then added to RPE1 cells grown one day before and incubated further at 37°C overnight. Cells were then spread onto fibronectin Cytoo chips (Cytoo Cell Architect) for 4h at 37°C with F-12 (with 10% (vol/vol) FCS (feotal calf serum), 10 mM Hepes, 100 units/ml of penicillin and 100  $\mu\text{g}/\text{ml}$  of Strep) before imaging. Cell adhesion on micropat-terns both constrains the cells in terms of lateral movement and averages their size and shape (1100  $\mu\text{m}^2$ ).

Live-cell imaging was performed using simultaneous dual color Total Internal Reflection Fluorescence (TIRF) microscopy. All imaging was performed in full conditioned medium at 37°C and 5%  $\text{CO}_2$ . Simultaneous dual color TIRFM microscopy sequences were acquired on a Nikon TE2000 inverted microscope equipped with a x100 TIRF objective (NA=1.49), an azimuthal (spinning) TIRF module (Ilas2, Roper Scientific), an image splitter (DV, Roper Scientific) installed in front of an EMCCD camera (Evolve, Photometrics) and a temperature controller (LIS). GFP and m-Cherry were excited with a 488 nm and a 561 nm laser, respectively (100mW). The system was driven by the Metamorph software (Molecular De-vices). A range of angles corresponding to a set of penetration depths is defined for a given wavelength and optical index of the medium ([Boulanger et al., 2014](#)). We performed simultaneous double-fluorescence image acquisition using RPE1 cells double transfected with Langerin-YFP and Langerin-mCherry or Rab11A-GFP and Langerin-mCherry. Im-age series corresponding to simultaneous two colors multi-angles TIRF image stacks were recorded at one stack of 12 angles every 360 ms during 14.76 s, with a 30 ms exposure time per frame. Three-dimensional reconstructions of the whole cells were performed on the first 300 nm in depth of the cells using a 30-nm axial pixel size, see [Boulanger et al. \(2014\)](#).

## E Supplementary Figure

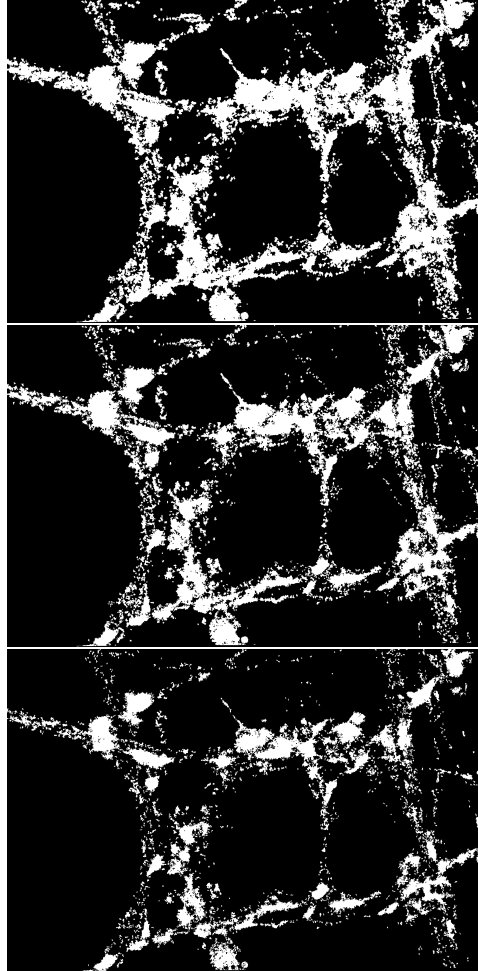


Figure S21: vGlut segmentations. Three different segmentations of purple channel of image shown in Figure 2 of the main manuscript.

## References

- Andreska, T., Aufmkolk, S., Sauer, M., and Blum, R. (2014). High abundance of BDNF within glutamatergic presynapses of cultured hippocampal neurons. *Front Cell Neurosci* **8**, 1–15.
- Andrews, D. W. (1991). Heteroskedasticity and autocorrelation consistent covariance matrix estimation. *Econometrica* **59**, 817–858.
- Basset, A., Boulanger, J., Salamero, J., Bouthemy, P., and Kervrann, C. (2015). Adaptive spot detection with optimal scale selection in fluorescence microscopy images. *IEEE T Image Processing* **24**, 4512–4527.
- Bolte, S. and Cordelieres, F. (2006). A guided tour into subcellular colocalization analysis in light microscopy. *J Microscopy* **224**, 213–232.
- Bolthausen, E. (1982). On the central limit theorem for stationary mixing random fields. *The Annals of Probability* **10**, 1047–1050.
- Boulanger, J., Gueudry, C., Munch, D., Cinquin, B., Paul-Gilloteaux, P., Bardin, S., Guérin, C., Senger, F., Blanchoin, L., and Salamero, J. (2014). Fast high-resolution 3D total internal reflection fluorescence microscopy by incidence angle scanning and azimuthal averaging. *Proc Natl Acad Sci USA* **111**, 17164–17169.
- Chiu, S. N., Stoyan, D., Kendall, W. S., and Mecke, J. (2013). *Stochastic geometry and its applications*. John Wiley & Sons, 3 edition.
- Comeau, J. W. D., Kolin, D. L., and Wiseman, P. W. (2008). Accurate measurements of protein interactions in cells via improved spatial image cross-correlation spectroscopy. *Molecular BioSystems* **4**, 672–685.
- Costes, S., Daelemans, D., Cho, E., Dobbin, Z., Pavlakis, G., and Lockett, S. (2004). Automatic and quantitative measurement of protein-protein colocalization in live cells. *Biophysical J* **86**, 3993–4003.
- Cressie, N. (1991). *Statistics for Spatial Data*. Wiley-Interscience.
- de Chaumont, F., Dallongeville, S., Chenouard, N., Hervé, N., Pop, S., Provoost, T., Meas-Yedid, V., Pankajakshan, P., Lecomte, T., Le Montagner, Y., Lagache, T., Dufour, A.,

- and Olivo-Marin, J.-C. (2012). Icy: an open bioimage informatics platform for extended reproducible research. *Nature Methods* **9**, 690–696.
- Dunn, K., Kamocka, M., and McDonald, J. (2011). A practical guide to evaluating colocalization in biological microscopy. *Am J Physiol Cell Physiol* **300**, C723–C742.
- Gidon, A., Bardin, S., Cinquin, B., Boulanger, J., Waharte, F., Heliot, L., de la Salle, H., Hanau, D., Kervrann, C., Goud, B., and Salamero, J. (2012). A Rab11A/Myosin Vb/Rab11-FIP2 complex frames two late recycling steps of Langerin from the ERC to the Plasma membrane. *Traffic* **13**, 815–833.
- Gotze, F., Heinrich, L., and Hipp, C. (1995).  $m$ -dependent random fields with analytic cumulant generating function. *Scandinavian J Statistics* **22**, 183–195.
- Guyon, X. (1995). *Random fields on a network: modeling, statistics, and applications*. Springer Science & Business Media.
- Helmuth, J., Paul, G., and Sbalzarini, I. (2010). Beyond co-localization: inferring spatial interactions between sub-cellular structures from microscopy images. *BMC Bioinformatics* **11**, 372.
- Lagache, T., Sauvonnnet, N., Danglot, L., and Olivo-Marin, J.-C. (2015). Statistical analysis of molecule colocalization in bioimaging. *Cytometry Part A* **87**, 568–579.
- Manders, E., Verbeek, F., and Aten, J. (1993). Measurement of co-localization of objects in dual-colour confocal images. *J Microscopy* **169**, Pt 3, 375–382.
- Møller, J. and Waagepetersen, R. P. (2004). *Statistical Inference and Simulation for Spatial Point Processes*. Chapman and Hall/CRC, Boca Raton.
- R Core Team (2017). *R: A Language and Environment for Statistical Computing*. R Foundation for Statistical Computing, Vienna, Austria.
- Ramirez, O., Garcia, A., Rojas, R., Couve, A., and Härtel, S. (2010). Confined displacement algorithm determines true and random colocalization in fluorescence microscopy. *Journal of Microscopy* **239**, 173–183.
- Schlather, M., Malinowski, A., Oesting, M., Boecker, D., Strokorb, K., Engelke, S., Martini, J., Ballani, F., Moreva, O., Auel, J., Menck, P. J., Gross, S., Ober, U., Christoph Berreth, Burmeister, K., Manitz, J., Ribeiro, P., Singleton, R., Pfaff, B., and R Core Team (2017). *RandomFields: Simulation and Analysis of Random Fields*. R package version 3.1.50.

- Schneider, C. A., Rasband, W. S., and Eliceiri, K. W. (2012). NIH Image to ImageJ: 25 years of image analysis. *Nat Methods* **9**, 671–675.
- Sherman, E., Barr, V., Manley, S., Patterson, G., Balagopalan, L., Akpan, I., Regan, C. K., Merrill, R. K., Sommers, C. L., Lippincott-Schwartz, J., and Samelson, L. E. (2011). Functional nanoscale organization of signaling molecules downstream of the T cell Antigen receptor. *Immunity* **35**, 705–720.
- Wu, Y., Eghbali, M., Ou, J., Lu, R., Toro, L., and Stefani, E. (2010). Quantitative determination of spatial protein-protein correlations in fluorescence confocal microscopy. *Biophysical Journal* **98**, 493–504.